Post-print version of the paper by Aune et al. in Int J Impact Eng, 108 (2017) 27-46
http://dx.doi.org/10.1016/j.ijimpeng.2017.04.001

On the dynamic response of blast-loaded steel plates with and without pre-formed holes

V. Aune[a,b,*], G. Valsamos[c], F. Casadei[c,1], M. Langseth[a,b] and T. Børvik[a,b]

[a] *Structural Impact Laboratory (SIMLab), Department of Structural Engineering, NTNU, Norwegian University of Science and Technology, NO-7491 Trondheim, Norway*

[b] *Centre for Advanced Structural Analysis (CASA), NTNU, NO-7491 Trondheim, Norway*

[c] *European Commission, Joint Research Centre (JRC), Directorate for Space Security and Migration, Safety and Security of Buildings, 21027 Ispra, Italy*

Abstract

The dynamic response of blast-loaded steel plates is studied both experimentally and numerically. The blast loading was generated using a shock tube facility. This is an alternative to explosive detonations where the blast intensity is easily controlled through the initial conditions in each experiment. Massive and deformable steel plates where located at the tube end during testing, where the massive-plate tests served as a basis for comparison with respect to fluid-structure interaction (FSI) effects. Special focus was placed on the influence of pre-formed holes on the dynamic response and failure characteristics of the deformable plates. The plates had an exposed area of $0.3\,\mathrm{m} \times 0.3\,\mathrm{m}$ and the tests covered a wide range of structural responses from large inelastic deformations to complete tearing along the diagonals of the plates. Numerical simulations were performed in the finite element code EUROPLEXUS, where the plate was uniformly loaded by the pressure measurements from the massive-plate tests. The plate deformation and the observed crack propagation were successfully recreated by using element erosion and adaptive mesh refinement in the plate, driven by the damage parameter in the material model. As expected, the simulations overestimated the plate deformations due to the underlying assumption that the blast pressure was uncoupled from the deformation (i.e., neglecting FSI). It was also found that the modelling of the realistic boundary conditions with clamping frames, contact and friction was essential to predict the experimental results.

Keywords: Airblast loading, perforated plates, ductile failure, adaptive mesh refinement (AMR), EUROPLEXUS.

* Corresponding author. Tel.: + 47-73-59-47-05; fax: + 47-73-59-47-01.

E-mail address: vegard.aune@ntnu.no (V. Aune).

[1] Retired.

1. Introduction

Even though blast events often involve perforated plates, the current literature indicates that there is limited research on the influence of holes on the dynamic response of such structures. Holes may be induced in plated structures for various applications and reasons, e.g. due to perforations in combined blast and fragmentation events [1] and pre-formed holes in façades or passive mitigation systems [2][3]. Rakvåg et al. [4] investigated the influence of pre-formed holes with different geometries on the response of medium-strength steel plates exposed to pressure pulse loading. Although the plates experienced large deformations, there were no signs of failure other than some localization of plastic deformation at the extremities of the holes. Veldman et al. [5] studied the response of pre-pressurized aluminium plates subjected to blast loading. The test panels were reinforced with aluminium extrusions attached to the plates using rivet joints. Consistent failure of the rivet joints motivated tests without reinforcement, but with the pre-drilled holes at the rivet locations, and it was found that the crack initiation emerged from these holes due to stress concentrations. Cracks were also found to originate at laser welded joints for thin steel sheets supported on a cellular metal foundation when exposed to blast loading in Ref. [6], resulting in complex failure patterns.

Several experimental and numerical techniques can be used to study the response of blast-loaded plates, where the focus is mainly on an accurate quantification of the loading and on the corresponding dynamic response. The most frequently used experimental techniques include the ballistic pendulum approach using e.g. sheet explosives [7], free-field airblast detonations at a given stand-off distance from the target [8][9] or shock tube experiments using either explosives [10] or compressed air [11][12] to generate the blast loading. Due to the complexity in both the blast loading and the resulting dynamic response, numerical techniques like the finite element (FE) method are often required for sufficient insight into the problem. The uncoupled approach is often the preferred procedure in today's blast-resistant

design [13]. The loading is then obtained using either empirical relations based on experimental observations or numerical simulations of the blast wave propagation in a fixed Eulerian reference frame. The underlying assumptions in the Eulerian framework are rigid boundary conditions and no deformation of the structure, and the simulations are typically performed in a computational fluid dynamics (CFD) code. Such codes compute the spatial and temporal pressure distribution along the plate surface. The obtained pressure histories are finally applied in a computational structural dynamics code to determine the corresponding dynamic response. The uncoupled approach therefore makes the inherent assumption that the blast properties are unaltered by the structural motion and vice versa.

The accuracy of the uncoupled approach is dependent on the blast and structural properties, since fluid-structure interaction (FSI) takes place if the structure is allowed to move or deform during the load duration. Taylor [14] suggested that lightweight structures undertake less momentum compared to heavier structures when exposed to the same blast intensity, indicating that the motion of the reflecting surface reduces the pressure acting on it. Subsequent work by Kambouchev et al. [15][16] showed that the benefit of FSI effects is marginal for blast waves with low intensities, but may be considerable for high-intensity blast waves. They also indicated that the use of lightweight structures may reduce the transmitted impulse from the blast wave, and argued that this could be exploited in structural designs for improved resistance. The results by Kambouchev et al. [15][16] were later used by Vaziri and Hutchinson [17] in the assessment of sandwich and monolithic metal plates subjected to an intense air blast. It was found that the plate deflection was reduced at larger blast intensities when considering FSI for lightweight structures. A coupled approach may therefore be necessary at larger blast intensities when evaluating the response of lightweight structures.

This study evaluates the performance of the uncoupled approach in predicting the dynamic response of blast-loaded plates. Shock tube tests are carried out to obtain the loading

on a massive plate and to study the dynamic response of thin steel plates under similar blast intensities. The capability of the uncoupled approach in predicting the experimental observations are then evaluated numerically using the FE code EUROPLEXUS (EPX) [18]. Special focus is placed on the influence of pre-formed holes on the dynamic response and failure characteristics of square plates. The investigated plates have similar geometry as those studied by Rakvåg et al. [4]. However, the shock tube used in this study facilitates a blast environment with much larger pressure magnitudes than in Ref. [4], resulting in complete failure of the plates. Recent advancements including adaptive mesh refinement in EPX [19] are used in combination with element erosion to predict the crack propagation observed in the experiments. Material tests were also performed to determine the material behaviour at large plastic strains and to identify the parameter in an energy-based failure criterion.

2. Experimental study

2.1. Experimental setup and programme

The blast tests were performed in the SIMLab Shock Tube Facility (SSTF) at NTNU. A detailed presentation of the overall shock tube design, functioning and an evaluation of its performance with respect to blast loading can be found in Aune et al. [12]. The SSTF has proven to be an easily controllable alternative to explosive detonations and can be used to study the dynamic response and fluid-structure interaction (FSI) of blast-loaded structures. This section is therefore limited to the experimental setup and programme used herein.

An illustration of the experimental setup, photographs of the SSTF and pictures of the test specimens are shown in Figure 1. The shock tube consists of a high-pressure chamber (called driver in Figure 1a and shown in Figure 1b) which is separated from a low-pressure chamber (denoted driven in Figure 1a) using several intermediate chambers separated by

diaphragms. A sudden opening of the diaphragms generates a shock wave moving into the low pressure chamber and rarefaction waves that expand into the higher pressure chamber. Using a relatively small ratio between the lengths of the two pressure chambers, this experimental setup differs from traditional shock tubes in the way that the reflected rarefaction waves catch up with the shock wave resulting in pressure profiles similar to that from explosive detonations (see Ref. [12]). The interaction between a planar blast wave and a structure may then be studied by placing a test specimen inside or at the end of the tube. The experimental setup used in this study is based on the findings in Aune et al. [12], where it was shown that the blast intensity is a function of both the driver-to-driven-length ratio and the driver pressure. It was therefore decided to use aluminium inserts to obtain a driver length of 0.77 m, while the driven section was operated with a total length of 16.20 m (Figure 1a).

The blast intensity is varied by changing the initial pressure in the driver section, while the initial pressure in the driven section is operated at ambient conditions. Table 1 gives the test matrix used herein, where each test is numbered XY-Z in which X denotes rigid plate (R), deformable plate without holes (D) or with pre-formed holes (P), Y indicates the firing overpressure in bars in the driver and Z is the test number. The massive steel plate was used to obtain a rigid blind flange (Figure 1d), while thin deformable plates (both with and without holes) were used to introduce moving boundary conditions (Figure 1e and f). Pressure measurements from the massive plate tests were used as basis to investigate potential FSI effects in the tests with deformable plates. Both the massive plate with thickness 0.05 m and the deformable steel plates with dimensions $0.625\,\mathrm{m} \times 0.625\,\mathrm{m} \times 0.0008\,\mathrm{m}$ were clamped to the end flange of the tube (Figure 1d-f) in an attempt to achieve fixed boundary conditions. The plates had an exposed area of $0.3\,\mathrm{m} \times 0.3\,\mathrm{m}$ (equal to the internal cross-section of the tube as shown in Figure 2). Two repetitive tests were performed for the plates with pre-formed holes to investigate possible variations in deformation histories and failure patterns.

Piezoelectric pressure sensors (Kistler 603B), corresponding charge amplifiers (Kistler 5064) and data acquisition system from National Instruments (NI USB-6356) were used to measure the pressure during the tests. Two sensors flush mounted in the tube wall measured the pressure behind the incident and reflected shock wave 24.5 cm (Sensor 2) and 34.5 cm (Sensor 1) upstream the test specimens (see Figure 1a). The pressure sensors were automatically triggered when the shock wave arrived at Sensor 1, and they were operated with a sampling frequency of 500 kHz. Moreover, the massive plate was equipped with 12 pressure sensors along the vertical, horizontal and diagonal to measure the pressure distribution on a rigid boundary. A thin layer of insulating silicone (Kistler 1051) was used to shield the pressure sensors against heat transfer from the shock wave during the tests.

2.2. DIC measurements

Three-dimensional digital image correlation (3D-DIC) analyses were used to measure the displacement field for all the 0.8 mm thick steel plates. Two Phantom v1610 high-speed cameras were positioned approximately 1.70 m from the plates in a symmetric stereovision setup, and the separation angle between the optical axes was approximately 73° (Figure 1a). The recording rate was chosen to 24 kHz in all tests with an exposure time of 30 μs and an image resolution of 768×800 pixels at 12-bit grey level digitization. The high-speed images were synchronized with the pressure measurements which enabled a thorough investigation of each test. The camera calibration and image analyses were carried out using an in-house FE-based DIC code (eCorr) with a mesh of Q4 elements [12][20]. Prior to each test, the plates were spray-painted white before a template was used to apply a black speckle pattern with a size distribution in the range of 2-4 mm, equivalent to 3.4-6.7 pixels (see Figure 1e-f). The choice of speckle size was based on minimizing the effect of aliasing in the DIC calculations [12]. A set of 2×2 checkerboard stickers glued to the clamping frame (see Figure 1e-f) was

used to measure the axial movement of the entire facility caused by large momentum changes induced in the gas during firing. These checkerboard stickers were observed by the two cameras during the test and the DIC code was used to provide the global movement in 3D space. All deformation profiles presented herein were corrected for this slight movement. Figure 3 illustrates a set of recorded images from test P25-02 by the two synchronized high-speed cameras with the resulting DIC meshes plotted on top. The corresponding 3D model showing out-of-plane displacements calculated using eCorr is also illustrated in the figure.

To avoid damaging the high-speed cameras and loss of calibration in the stereovision setup, the tank was closed during the tests of the plates with pre-formed holes (see Figure 1a). Failure was not expected in the experiments of the thin steel plates without holes and the tank was therefore kept open during these experiments (see Figure 1c). The camera calibration and the 3D-DIC technique were validated by Aune et al. [12] using a laser displacement sensor (optoNCDT 2310-50) in a similar experimental setup. The measured mid-point deflections based on the laser and the 3D-DIC were in excellent agreement, and the 3D-DIC technique is therefore considered well suited to measure the displacements during these tests.

2.3. Material

The 0.8 mm thick plates were manufactured from steel sheets of type Docol 600 DL produced by Swedish Steel Ltd. (SSAB) [21]. This material provides a two-phase structure of ferrite and martensite obtained by heat treatment, where the ferrite gives the ductile properties and the martensite gives the strength. The nominal chemical composition of the material can be found in Holmen et al. [22], while the nominal yield stress and ultimate tensile strength were given by the manufacturer to be 299 MPa and 677 MPa, respectively.

Uniaxial tensile tests were carried out on dog-bone specimens with the same geometry as in Ref. [23] cut from the sheets. The tests were performed in a Zwick/Roell Z030 testing

machine at a constant deformation rate of 2.1 mm/min. This corresponds to an initial strain rate of $\dot{\varepsilon} = 5\times10^{-4}$ s^{-1} for a gauge length of 70 mm. Three parallel tests were performed in three different directions ($0^\circ, 45^\circ, 90^\circ$) with respect to the rolling direction of the plate. Two-dimensional digital image correlation (2D-DIC) [20][24] was used to measure the displacement field and these recordings were synchronized with the force measured by the hydraulic test machine at a sampling rate of 4 Hz for all tests. A virtual extensometer of 50 mm initial gauge length L_0 was used to obtain the elongation history $u(t)$ based on 2D-DIC. To validate the DIC measurements, the first test in each direction was instrumented with an extensometer to measure the elongation over the same initial gauge length (50 mm). The DIC measurements and the extensometer showed excellent agreement, and only the DIC recordings are therefore used in the following.

Force-elongation curves from the tensile tests are shown in Figure 4a. It is seen that the steel is slightly anisotropic both in flow stress and elongation to failure. This is most evident in the 45° and 90° directions. However, Gruben et al. [25] showed that plastic anisotropy in Docol 600 DL can be neglected. This was further confirmed by Aune et al. [9], which showed that the material can be considered as isotropic with moderate strain-rate sensitivity. The true stress σ, true strain ε and true plastic strain ε^p before necking are found using the relations

$$\sigma = \sigma_e(1+\varepsilon_e), \quad \varepsilon = \ln(1+\varepsilon_e), \quad \varepsilon^p = \varepsilon - \frac{\sigma}{E} \tag{1}$$

where σ equals the equivalent stress σ_{eq} before necking, ε^p corresponds to the equivalent plastic strain p in a uniaxial tension test, E is Young's modulus, and the engineering stress σ_e and strain ε_e are given by

$$\sigma_e = \frac{F}{A_0}, \quad \varepsilon_e = \frac{u}{L_0} \tag{2}$$

where A_0 is the initial cross-sectional area in the gauge region. Figure 4b shows the equivalent stress-plastic strain curve for a representative test in the rolling direction (0°) until necking.

3. Experimental results

3.1. Pressure measurements

FSI effects could be investigated experimentally by comparing pressure histories at Sensor 2 in the massive and deformable plate tests with the same initial conditions. This is presented in Figure 5. No low-pass filtering was used on the experimental data. It should be noted that there is a rather complex wave pattern inside the tube during the test, where the wave fronts will interact and continue back and forth in the tube until a static overpressure is reached when the gas comes to rest (see Ref. [12]). This is observed as multiple peaks (secondary and tertiary reflections) of decreasing magnitude on the pressure measurements and leads to multiple impacts on the plate such that the final configuration may not be representative for the primary loading event. However, the relevant timescale of the experiment depends on the application. The time-window of interest in these experiments is limited to the positive phase of the blast load.

The pressure sensors first record the incident overpressure p_{so} just before impact and then the reflected overpressure p_r after impact when the blast wave travels back towards the driver (see Figure 5). It is observed that the incident (side-on) pressure is in excellent agreement between tests with similar firing conditions, while there is a reduction in the reflected pressure for the deformable plates. The deformable plates without holes result in a small reduction of the peak reflected overpressure, while the subsequent flow seems to be barely altered when allowing for finite deformations (except for test D15-01 in Figure 5b). It

is important to emphasize that Sensor 2 is located 24.5 cm upstream the test specimen flush mounted in the inner wall (see Figure 1a), and that the peak reflected overpressure immediately after reflection is often assumed to be independent of the stiffness of the test object (see e.g. Ref. [26]). The effect of the pre-formed holes is an additional reduction of the pressure upstream the test specimen. This decrease in pressure may imply a reduced pressure in the vicinity of the holes. However, Figure 5 indicates that most of the pressure remains in front of the plate. The noticeable decrease in pressure in tests P35-01 and P35-02 is due to a complete failure of the plates in these tests. As soon as the plate is completely removed from the tube end, the pressure is allowed to enter freely into the expanding tank volume. This results in a left-running rarefaction wave and is recorded as a sudden drop in pressure at Sensor 2 (Figure 5d).

3.2. Response of blast-loaded plates

Figure 6 shows the mid-point deflection histories measured with 3D-DIC for the deformable plates without holes (Figure 6a) and representative plates with holes (Figure 6b). The corresponding maximum deflection $d_{z,max}$, permanent deflection $d_{z,p}$ and maximum velocity $v_{z,max}$ at the mid-point of the plates are summarized in Table 2. All curves are corrected for the rigid body movement of the shock tube, and also shifted in time to match the time of impact and simplify the comparisons. The repetitive tests for the perforated plates showed excellent agreement both in pressure and deformation histories. Therefore, only one of these tests is reported in the following.

All deformable plates experienced inelastic deformations with a permanent deflection in the same direction as the incident blast wave, and the elastic rebound became smaller as the load intensity increased (Figure 6). It was also observed an increased mid-point deflection for the perforated plates (Figure 6b) compared to the plates without holes (Figure 6a) under

similar loading conditions. The perforated plates also involved larger oscillations after the elastic rebound, while the difference $\Delta d_{z,exp}$ between the maximum mid-point deflection $d_{z,max}$ and the permanent mid-point deflection $d_{z,p}$ was found to be approximately the same for the deformable plates with similar loading conditions (see Table 2). There were no visible signs of tearing at the boundaries for the plates without holes. However, failure was observed in all tests involving perforated plates, except for tests P05-01 and P05-02. Cracks initiated at the corners of the pre-formed holes and propagated along the diagonals of the plates where the extent of the crack growth was dependent on the intensity of the loading. This is illustrated in Figure 7, where high-speed images of representative tests at the time of maximum deflection are shown. It is observed that the tests cover the entire range from no visible signs of failure in tests P05-01 and P05-02 (Figure 7a), crack initiation at the extremities of the holes in P15-01 and P15-02 (barely seen in Figure 7b), to noticeable crack growth along the diagonals of the plates in P25-01 and P25-02 (Figure 7c) and, finally, complete failure along the diagonals in P35-01 and P35-02 (Figure 7d). Figure 8 shows the failure process in test P35-02 in more detail, where it is observed that the crack propagation is nearly symmetric (Figure 8a-b) until the cracks meet in the centre of the plate (Figure 8c-d). After the cracks have met in the centre (Figure 8c), the cracks propagate towards the outer corners of the plate boundary resulting in complete tearing (Figure 8d). The average crack tip velocities in tests P35-01 and P35-02 were estimated to be 137.1 m/s (62.0 m/s) and 88.4 m/s (64.3 m/s), respectively. These are the average crack tip velocities along the diagonals at the centre of the plates (Figure 8c), while the values in parentheses are the average crack tip velocity from the outer extremity of the hole towards the corners of the plate boundary (Figure 8d). A plausible explanation for the crack propagation along the diagonals of the plates may be a reduced pressure in the vicinity of the holes. This will result in a larger pressure at the plate centre and may force the crack to propagate along the diagonals. Since it is challenging to conclude on the influence of the pre-

formed holes on the observed crack propagation in the tests with perforated plates, this will be investigated numerically in Section 5.

4. Material modelling

4.1. Constitutive relation

Blast-loaded plates typically experience large strains, elevated strain rates, temperature softening and ductile failure. Since the material proved to be isotropic (see Section 2.3), the von Mises yield criterion assuming associated flow and isotropic work hardening was considered appropriate to model the material behaviour. This is accounted for by the *VPJC* material model in the EPX code [18], which uses a generalized form of Hooke's law for the elastic behaviour and a modified Johnson-Cook relation for the flow stress [27]. The dynamic yield function f_{d} is then given by

$$\begin{aligned} f_d(\boldsymbol{\sigma}, p, \dot{p}, T) &= \sigma_{eq}(\boldsymbol{\sigma}) - \sigma_y(p,T)\left[1+\frac{\dot{p}}{\dot{p}_0}\right]^c \\ &= \sqrt{\frac{3}{2}\boldsymbol{\sigma}':\boldsymbol{\sigma}'} - \left[\sigma_0 + \sum_{i=1}^{2} Q_i(1-\exp(-C_i p))\right]\left[1+\frac{\dot{p}}{\dot{p}_0}\right]^c\left[1-T^{*m}\right] \end{aligned} \tag{3}$$

where σ_{eq} is the von Mises stress, $\boldsymbol{\sigma}$ is the Cauchy stress tensor, σ_y is the flow stress, p is the equivalent plastic strain, $\dot{p}$ is the equivalent plastic strain rate, $\dot{p}_0$ is a user-defined strain rate, σ_0 represents the initial yield stress, (Q_i, C_i, c, m) are material constants and $\boldsymbol{\sigma}'$ is the deviatoric part of the Cauchy stress. The homologous temperature is defined as $T^* = (T - T_r)/(T_m - T_r)$, where T is the absolute temperature, T_r is the ambient temperature and T_m is the melting temperature of the material. Since the dynamic response in blast environments is very rapid, the temperature evolution in time is assumed to be adiabatic and calculated based on the plastic dissipation as

$$\dot{T} = \frac{\chi}{\rho C_p} \sigma_{eq} \dot{p} \tag{4}$$

where χ is the Taylor-Quinney coefficient, ρ is the density and C_p is the specific heat capacity of the material. The Taylor-Quinney coefficient represents the fraction of plastic work converted into heat, while the remaining fraction is energy stored in the material due to structural rearrangements. A detailed presentation of the *VPJC* material model is given in Ref. [27].

4.2. Failure criterion

The *VPJC* material model allows for ductile failure through the Cockcroft-Latham (CL) criterion [28], which is an energy-based criterion using the "plastic work" per unit volume to predict failure. The criterion is assumed uncoupled from the constitutive equations, so that

$$D = \frac{W}{W_c} = \frac{1}{W_c} \int_0^p \langle \sigma_1 \rangle \, dp \tag{5}$$

where D is the damage variable. The critical CL parameter W_c is found by integrating the major principal stress σ_1 from a uniaxial tension test over the entire equivalent plastic strain path until the plastic strain at failure p_f is reached. The Macaulay brackets imply that only positive values of the major principal stress contribute to the damage evolution. Moreover, by using an alternative expression for the major principal stress

$$\sigma_1 = \sigma_H + \frac{3+\mu_\sigma}{3\sqrt{3+\mu_\sigma^2}} \sigma_{\text{eq}} = \left(\sigma^* + \frac{3+\mu_\sigma}{3\sqrt{3+\mu_\sigma^2}} \right) \sigma_{\text{eq}} \tag{6}$$

it is observed that the CL failure criterion accounts for both the stress triaxiality σ^* and the Lode parameter μ_σ defined by

$$\sigma^* = \frac{\sigma_H}{\sigma_{eq}}, \quad \mu_\sigma = \frac{2\sigma_2 - \sigma_1 - \sigma_3}{\sigma_3 - \sigma_1} \tag{7}$$

where $\sigma_1 \geq \sigma_2 \geq \sigma_3$ are the ordered principal stresses and $\sigma_H = (\sigma_1 + \sigma_2 + \sigma_3)/3$ is the hydrostatic stress. Thus, the underlying assumption for the CL criterion is that damage is driven by the plastic work amplified by a factor depending on the stress state through σ^* and μ_σ.

Material failure occurs when the damage parameter D in Eq. (5) reaches unity. Previous studies in e.g. terminal ballistics [29][30][31][32] have demonstrated the robustness of the CL criterion. It is also worth noting that experimental studies by Langdon et al. [33] on blast-loaded plates indicated that the failure of ductile materials could be related to the specific energy giving tensile failure. This suggests that failure under blast-load conditions could be predicted from simple quasi-static tension tests.

4.3. Identification of material parameters

The material tests presented in Figure 4a deviate slightly from the results of other batches and thicknesses of the same material (see Refs. [4][23][25][22]). It was therefore considered necessary to identify the quasi-static material parameters (σ_0, Q_i, C_i) for the material used in this study. The calibration was performed in a similar way as in Ref. [27], where the parameters of the extended Voce hardening rule (σ_0, Q_i, C_i) were obtained by inverse modelling of the material test using the optimization package LS-OPT [34]. LS-OPT can be used to minimize the mean-squared error between experimental and numerical results for a predefined target curve through sequential analyses on the same FE model with varying input parameters. It was convenient to establish the FE model in LS-DYNA [34] due to its tailored interface with LS-OPT. The FE model consisted of Belytschko-Tsay shell elements with an initial element size in the gauge region equal to the specimen thickness in an attempt to capture local necking, and the force-elongation curve from a typical tensile test in the rolling (

0°) direction was chosen as the target curve. The boundaries of the FE model were subjected to the same elongation history as in the test, where the velocity from the test was ramped up over the first 1.0 % of the total computational time using a smooth transition curve. Mass-scaling by a factor 10^9 was used to speed up the computational time. Larger scaling factors resulted in non-physical inertia effects during the necking and a non-negligible kinetic energy in the simulations. Material parameters from LS-OPT are listed in Table 3, while physical constants and the remaining material parameters were taken from Refs. [25][22][27] and provided in Table 4. The initial yield stress σ_0 was defined as the stress at 0.2 % plastic strain in the representative test.

A separate analysis with the exact same mesh and the shell elements to be used in the simulations of blast-loaded plates was performed in EPX to verify that the material parameters were applicable also in this FE code. Figure 4a compares the force-elongation curves from the material tests and the simulation in EPX with the optimized material parameters, while Figure 4b compares equivalent stress - plastic strain curves until necking from a representative test with the analytical expression in the first term of the flow stress in Eq. (3) using the data from Table 3. It is observed that the optimised material parameters are able to describe the overall response and material behaviour very well.

The CL parameter W_c in Eq. (5) was determined from the same simulation by inspecting the element exposed to the largest plastic work W. It is emphasized that the W_c parameter found from this approach is mesh-size dependent, since the element of interest is always located inside the neck where the representation of necking is influenced by the mesh size [38]. Only the tension test in the rolling direction of the plate was used in the calibration. This implies a possible spread in W_c between each material direction, which may affect the numerical result. However, modelling of anisotropic failure is beyond the scope of this study.

The point used to extract W_c from the numerical result is indicated by a red dot in Figure 4a, and the value is given in Table 3. Figure 4a shows that the numerical model captured the localized necking. The CL parameter W_c was therefore determined at the same force level as when failure occurred in the test.

5. Numerical simulations

5.1. Finite element code

The numerical simulations were performed by the explicit FE code EUROPLEXUS (EPX) [18], which is jointly developed by the French Commissariat à l'Energie Atomique et aux Energies Alternatives (CEA) and the Joint Research Centre of the European Commission (JRC). EPX solves the conservation of momentum (equilibrium) equations in the structural sub-domain and the conservation of mass, momentum and energy in the fluid sub-domain. The fluid is considered as compressible and inviscid (Euler equations). In the simulations presented in this paper, only the structural domain has been included. The Cast3M code [35], also developed by CEA, was used to generate the FE meshes for the various numerical models, while the ParaView software [36] and EPX itself were used for post-processing of the numerical results.

5.2. Structural model

The structure was modelled by FEs using a Lagrangian description. Four-node shell elements were used for the plate, while eight-node brick elements were used for the clamping assembly when this was included in the FE model. The material was modelled using the *VPJC* model, already presented in Section 4.

In EPX, damage-based adaptive mesh refinement (AMR) can be activated in the plate according to a threshold criterion. When a monitored parameter, typically the damage D, reaches a chosen value $D_{\min}$, the shells are refined by splitting each element into four smaller elements using the technique of Ref. [19]. The mesh refinement strategy is shown in Figure 9 for a quadrilateral. During the refinement process hanging nodes are created in the transition zones at the interior of the body, e.g. h_1 and h_2 in Figure 9a. Their motion is constrained by the motion of the corresponding base nodes by means of suitable link conditions. Similarly, boundary-hanging nodes (b_1 and b_2 in Figure 9a) may appear. These automatically inherit any boundary conditions prescribed on the corresponding base nodes. Successive refinements then occur recursively, i.e., the maximum prescribed level $L^s_{\max}$ (minimum size of the elements) is applied where the damage reaches a chosen value $D_{\max} > D_{\min}$. The base elements in the initial unrefined mesh are conventionally assigned a level $L_0 = 1$, and at each refinement the level is incremented by 1 and the element size is halved. Since damage is monotonically increasing, a refined structure mesh is never unrefined. An element erosion algorithm is activated to remove the fully-damaged elements when $D = 1$ from the calculation. AMR is also crucial in order to reduce the structural mass lost in the calculation due to the element erosion process.

5.3. Contact formulations

In some of the performed simulations the numerical model also included the clamping assembly used to mount the plate to the end flange of the shock tube. The plate was placed between two relatively thick frames, connected by threaded bolts/nuts passing across holes in the plate as shown in Figure 2 and subjected to a given torque. To model the contact between the plate, the clamping frames and the bolts, the pinball contact/impact model (PINB) [39],

see Figure 10, was chosen. This algorithm was originally designed for impact and may not be as well suited to represent planar contact like in the present case. However, it was chosen here because of its robustness in detecting contact in even the most complex geometrical configurations. Two alternative formulations of the pinball contact model are available in EPX, a strong one (based on velocity constraints and Lagrange multipliers) and a weak one (based on a direct penalty method). The penalty formulation was chosen here for its simplicity and numerical efficiency, but also because it simplifies the treatment of friction by a simple Coulomb method.

To increase the spatial resolution for the contact detection and to better approximate flat contact, a hierarchic pinball method was chosen [40], see Figure 11. The parent pinballs initially embedded in the elements, and which interpenetrate each other, are progressively refined until a given size (diameter) of the spheres is reached. In the present flat contact configuration, this produces a huge number of pinball interpenetrations and corresponding contact constraints, which would challenge the use of a strong (implicit) contact method with Lagrange multipliers. However, the chosen penalty method does not suffer from this limitation, since it is completely explicit and does not require the solution of a linear system of equations for the constraints.

5.4. Terminology

To avoid confusion, we define some terminology used in the following description of the numerical model and results. By *massive* plate we indicate a plate (without holes) so thick that it behaves as rigid. Such a plate was used in some experiments to obtain the blast loading, but not in the simulations. Deformable (thin) plates are subdivided into *full* plates (no holes) and *perforated* plates (with pre-formed holes). Then, concerning modelling of the plate mounting boundary conditions, we distinguish between *fixed* plates and *clamped* plates. The former

model includes only the central (square) plate area exposed to the blast pressure and is completely blocked (both in translation and in rotation) along the perimeter. The latter model represents the entire plate, including the outer part between the two frames, and simulates the clamping by contact with friction under an assigned clamping pressure. Finally, by *on-plate pressure* we indicate the pressure measured directly on the loaded face of the massive plate. Note that in the experiments with deformable plates, the pressure is only measured at the tube wall at a certain distance from the loaded plate (i.e., at Sensor 2 in Figure 1a).

5.5. Numerical models

The objective of the present study has been to investigate the capability of predicting the structural response of the blast-loaded plates by using the measured on-plate pressure defined in Section 3 as input. Therefore, a Lagrangian description can be applied. This greatly simplifies and shortens the calculations with respect to a fully coupled FSI model including the fluid. This further enables us to focus on important structural aspects such as damage and failure, and on the influence of the boundary conditions on the dynamic response.

Figure 12 depicts the assembly of the numerical model. Thanks to the two symmetry planes in the experimental setup, it is sufficient to model only one quarter of the assembly (1/4 model). This reduces the computational time by almost a factor of 4 without deteriorating the quality of the results. The specimen can either be the full plate (Figure 12a) or the perforated plate (Figure 12b). Figure 12c-d illustrate the complete (4/4) model for the two different specimens, obtained by mirroring across the symmetry planes. The complete model is only used for visualization purposes and not for the simulation itself. Figure 12e-h illustrate the assembly of the various model components. The first component is the rear steel mounting frame with the attached bolts, fully blocked at its back surface. Assuming that the rear frame and the bolts behave as one body simplifies the model since there is no need to represent the

nuts nor to consider the contact between nuts and bolts. The second component is the plate (either full or perforated), and finally the front steel mounting frame, which contains holes for the passing bolts, is added. The pre-stress in the bolts was replaced in the model by an equivalent external pressure acting on the contact area between the nuts (not included in the model) and the front frame, seen as the yellow zones in Figure 12h. The applied clamping pressure was calculated according to Ref. [37], where the pre-tensioning force on each bolt was determined from the formula $F_p = M_t / (k\phi)$. Here, M_t (200 Nm) is the initial torque applied to each nut, k is the friction coefficient between nut and frame, and ϕ is the bolt diameter. The friction coefficient k depends on the thread geometry, and may vary between 0.10 and 0.23 [37]. The value 0.18 was selected based on recommendations in the literature [27][37]. The clamping pressure was applied on the nut contact area A_{nut} (yellow zone on the front frame), found to be 1060 mm² for each nut. Dividing the pre-tension force ($F_p = 46.6$ kN) on each bolt by the contact area A_{nut} resulted in a clamping pressure of 44 MPa, which was assumed constant with time.

The contact between the plate, the steel frames and the bolts was modelled using hierarchic pinballs in a weak approach based on a direct penalty method. Three different bodies were identified for the pinballs definition. The first body is the rear frame with the attached bolts, the second is the plate and the third is the front frame. Direct contact between the two frames was excluded to speed up the calculation. Friction between the bodies was activated by a simple Coulomb method. The friction coefficient between the clamping frames and the plate was set to 0.5 (both static and dynamic coefficients), a typical value from the literature for steel-to-steel interface. The plate was modelled by shell elements with 6 dofs per node using both the 4-node element *Q4GS* (see [18]) with 20 integration points (4 in the plane, 5 through the thickness) and the 3-node element *T3GS* with 5 integration points (1 in the plane, 5 through the thickness). The bolts and the clamping frames were represented by

solid elements with 3 dofs per node using both the 8-node brick element *CUB8* with 8 integration points and the 6-node wedge element *PR6* with 6 integration points. The clamping pressure was imposed via 4-node boundary condition elements *CL3D*. These elements automatically recognize the solid elements to which they are attached and use the assigned pressure histories.

The blast loading was applied using the idealized on-plate pressure histories presented in Figure 13, having similar blast intensities as in the deformable plate tests. That is, the loading measured at the massive plate in test RY was assumed to be valid also for tests with deformable plates without (DY) and with (PY) pre-formed holes. The modified Friedlander equation is typically used to represent the pressure history when the parameters governing the positive phase of blast load are known [12][27], i.e.,

$$p_r(t) = p_1 + p_{\mathrm{r,max}}\left(1-\frac{t-t_a}{t_{d+}}\right)\exp\left(\frac{-b(t-t_a)}{t_{d+}}\right), \qquad t_a < t < t_a + t_{d+} \tag{8}$$

where $p_{\mathrm{r,max}}$ is the peak reflected overpressure, p_1 is the ambient pressure, t_a is the time of arrival of the blast wave at the target, $t_{\mathrm{d+}}$ is the duration of the positive phase and b is the exponential decay coefficient. The positive specific impulse $i_{\mathrm{r+}}$ has an analytical solution given by

$$i_{r+} = \int_{t_a}^{t_a+t_{d+}} p_r(t)dt = \frac{p_{\mathrm{r,max}}t_{d+}}{b^2}\left[b-1+\exp(-b)\right] \tag{9}$$

The blast parameters $p_{\mathrm{r,max}}$, $t_{\mathrm{d+}}$ and $i_{\mathrm{r+}}$ may then be used to iteratively find the exponential decay coefficient b using Eq. (9). This enables the corresponding Friedlander curve to be expressed by Eq. (8). The pressure measurements from the RY tests were therefore idealized by curve-fitting to the Friedlander equation using Eqs. (8)-(9) and imposed as a uniformly distributed pressure on the exposed area of the plate (in magenta in Figure 12h). Thus, the underlying assumption is that the pressure is unaltered during the deformation of the plate

(i.e., an uncoupled approach). As can be seen from Figure 5, the pressure measured at a short distance upstream the plate (Sensor 2) in the massive plate tests is always higher than in the tests using deformable plates. The on-plate pressure was used in the numerical simulations since it was the only one measured directly at the specimen location, but one can expect that this will overestimate the actual pressure if the plate deforms. Like for the clamping pressure (when included in the model), the blast pressure on the exposed area of the specimen was modelled by *CL3D* boundary condition elements. The idealized pressure histories in Figure 13 are already reported in terms of the blast parameters in Eq. (8) in Ref. [12], but the parameters are also repeated in Table 5 for the completeness of this study.

A simplified model of the experimental setup, i.e., a fixed plate as illustrated in Figure 14, was also tested to investigate the influence of the boundary conditions. This model contained only the exposed area of the plate, with all nodes along the perimeter blocked both in translation and in rotation. Also in this case, only one quarter of the setup was modelled by exploiting the two symmetry planes. For all steel parts the *VPJC* material model presented in Section 4 was used. Table 3 and Table 4 list the material properties used in the numerical simulations.

5.6. Numerical results

A mesh sensitivity study showed that a mesh size of 10 mm in the plate is adequate to predict the global deformation observed in the experiments. However, the plate was modelled using a FE discretization of approximately 6 mm element size as the base mesh, in an attempt to predict the crack propagation in the cases that experienced failure by using local refinement techniques. The numerical results of the thin steel plates were compared to the experimental data in terms of mid-point deflection histories. The influence of the boundary conditions was also investigated by comparing the results from the two different approaches (simplified

model or clamped assembly model with contact and friction). The simplified models in Figure 14 were also used to indicate the characteristic loading domain in the tests (both full and perforated plates). This was estimated using the ratio between the positive phase duration t_{d+} in Table 5 and the natural period of vibration T_n in the plates. The natural period of vibration T_n was estimated to be 12.5 ms and 12.9 ms in the full and perforated plate, respectively. These estimates were in good agreement with a value of 13.9 ms found for an equivalent SDOF model of a square full plate with fixed boundary conditions based on Biggs [41]. According to these assumptions, the ratio t_{d+} / T_n ranged from 2.3 to 5.9 and from 2.2 to 5.7 for the full and perforated plate tests, respectively. Based on Baker et al. [42], the loading can then be classified as dynamic which indicates that the response is significantly influenced by the profile of the load history. This also justifies the use of numerical methods in the assessment of the global deformation in these tests due to the overlapping of the response and the positive phase duration [43].

5.6.1. *Full plates*

The results obtained from the numerical simulations for the full plate model are illustrated in Figure 15 in terms of mid-point deflection versus time, while the corresponding maximum deflection $d_{z,max}$, permanent deflection $d_{z,p}$ and maximum velocity $v_{z,max}$ at the mid-point of the plates are summarized in Table 2. Negative values of Δd_z imply that $d_{z,max}$ was larger in the simulation compared to the corresponding experiment. A comparison between the numerical approaches (using either fixed or clamped plates) and the experimental data is shown. Both the maximum $d_{z,max}$ and the permanent $d_{z,p}$ mid-point deflections were overestimated in the simulations, compared to the corresponding experiment (Table 2). To some extent this was expected, since the applied pressure load was conservative (i.e., higher

than the actual one). There is also a trend for the deviation to increase at higher blast load intensities. Both the clamped assembly and the simplified (fixed) model predicted velocities that were similar to the experimental observations. It is also observed that the results for the simplified (fixed) model are actually closer to the experimental data in this case, but only because in-plane sliding of the plate (which is unrealistic and contrary to observation) is restrained. This partially compensates for the increased mid-point deflection caused by the overestimated on-plate pressure. The increasing deviation between numerical and experimental data with increasing load intensity indicates that for the full plate tests the response cannot always be predicted by using the conservative loading from the massive plate tests. Including FSI effects might be important for the full plate model at the highest load intensities. It should be noted that the exposed area for the full plates is 16 % larger than the one for the perforated plates. Therefore, overestimation of the pressure can have a higher influence on the full plates, since the overall force is given by the pressure times the exposed plate area.

5.6.2. *Perforated plates*

Perforated plates are weaker than full plates and thus undergo higher deformations for the same loading. Moreover, the perforated plates experienced local damage, ranging from small crack initiations for the P25 tests to total tearing along the diagonals for the P35 tests. Figure 16 compares the experimental observations and the numerical results for all load intensities, while the corresponding maximum deflection $d_{z,max}$, permanent deflection $d_{z,p}$ and maximum velocity $v_{z,max}$ at the mid-point of the plates are summarized in Table 2. There is a very good agreement between the experimental data and the numerical results for all tests except for test P35, where the mesh size of 6 mm could not reproduce the total tearing along the main diagonals observed in the experiments. Note that the P35 experimental curve, hardly visible in

Figure 16, is suddenly interrupted due to tearing of the plate centre after about 1.75 ms. It is also observed that the mid-point deflection curves of perforated plates oscillate more than those of full plates. Thus, the time needed to reach final permanent deformation is longer.

Keep in mind that the applied loads, taken from the massive plate tests and used in the numerical simulations, are overestimated (conservative) for deformable plates. Therefore, the computed mid-point deflection and maximum velocity are expected to be higher than the experimental observations. However, in some simulations using the simplified (fixed) model these values were slightly lower than the corresponding experiment (observed as positive values of Δd_z in Table 2). The reason is believed to be that the simplified model fully restrains the exposed part of the plate and does not allow any sliding at the support. For the clamped assembly model the permanent mid-point deflections and maximum velocities were slightly higher than the experimental observations, as expected. The good general agreement between the experimental data and both numerical approaches indicates minor effects of the boundary conditions in the perforated plate tests. However, even though the numerical results were encouraging, neither the clamped assembly nor the simplified model was able to predict the failure observed in the P35 test. This indicates that a mesh size of 6 mm is too large to capture the strain localization leading to crack initiation, propagation and finally total tearing of the plate.

Therefore, a parametric study on the influence of the mesh size on the damage evolution was performed. Having verified the minor influence of the boundary conditions in the perforated plate tests, the investigation process can be greatly accelerated by using the simplified (fixed) model for the plate. Since a uniform mesh size of 6 mm was too large to predict the crack growth, finer meshes were also studied. The uniformly refined models used sizes of 1.50, 1.25, 1.00 and 0.75 mm. A smaller mesh size than 0.75 mm was not considered since this is at the order of the plate thickness (0.80 mm). Using shells with a size smaller than

their thickness is against the theory and the results may not be reliable. Failure by element erosion was introduced when the damage parameter D in Eq. (5) reached unity at all Gauss points of an element. Figure 17 illustrates the influence of the mesh size on the crack growth for test P35, where the damage value is presented for the various mesh sizes and for different time steps. For all mesh sizes, damage localized along the main diagonal (from right top to left bottom of the hole). Localization of damage was also observed along the other diagonal of the hole (from left top to right bottom), but of smaller magnitudes. It is evident that larger elements diffuse the failure process. This is expected due to the discrete nature of the FE method. Although minor cracks were initiated at mesh sizes of 1.50, 1.25 and 1.00 mm, a mesh size of 0.75 mm was found necessary to recreate the crack growth observed in the experiments. Figure 18 compares the damage evolution between test P35 and the numerical model for this mesh size. The comparison illustrates that not only the final state, but also the overall propagation of the cracks, is in good agreement. A simulation with a 0.75 mm mesh was also carried out for test P25 because this test was at the limit between initiation and growth of the cracks. Figure 19 compares results from test P25 and the 0.75 mm mesh size model. It is observed that the crack initiation was slightly underestimated in the simulation, but again the overall agreement between experimental results and numerical predictions was very good.

Thus, the uniformly refined model with a mesh size of 0.75 mm was able to predict the damage evolution for the perforated plate tests. However, using such a densely meshed model increased the CPU cost significantly, and both the CPU time and the memory usage reached a level that made the model difficult to handle. This would be even more challenging by adding complexity to the model, such as including the clamping frames or by considering a fully coupled FSI calculation involving the fluid. This motivated the use of a numerical technique that can reduce the size and cost of the model without sacrificing the accuracy of the results.

Such local mesh refinement methods are assumed to predict strain localizations with much less CPU requirements.

The damage-based AMR available in EPX was therefore employed in the following. An initial coarse (base) mesh is then automatically refined only in the zones where the damage parameter is within a user-defined threshold ($D_{\min} \le D \le D_{\max}$). As presented in Section 5.2, this algorithm splits the parent element into descendants, driven by the value of the damage parameter. It is emphasized that for this approach to predict localization of damage, the mesh should be refined relatively long before the element is eroded. A parametric study was therefore carried out to investigate the influence of the initial (base) mesh size L_{base}, the lower threshold value $D_{\min}$, the upper threshold value $D_{\max}$ and the maximum refinement level $L^s_{\max}$ on the localization of damage in the P35 test.

The definition of $L^s_{\max}$ is rather straightforward. It is related to the size of the base element L_{base} and to the size of the smallest element after maximum refinement L_{UR} (0.75 mm in this study). Two different base mesh sizes were investigated, one with $L_{\text{base}} = 3$ mm ($L^s_{\max} = 3$) and one with $L_{\text{base}} = 6$ mm ($L^s_{\max} = 4$). Both sets of parameters lead to the same minimum element size of 0.75 mm. The definition of the threshold range ($D_{\min}, D_{\max}$) was subjected to a parametric study to select the pair which best combined the failure mode prediction and the CPU time reduction. Figure 20 depicts contour maps (iso-values) of the damage parameter for the two most extreme threshold ranges tested in the fully refined 0.75 mm uniform mesh model, corresponding to $0.01 < D < 0.02$ and $0.10 < D < 0.20$, respectively. The figure refers to test P35, which results in complete tearing of the plate, and to a time instant shortly before crack initiation. As expected, the mesh must be refined relatively early, and well before element erosion, to capture the localization and crack propagation correctly since crack growth is a very fast phenomenon. For example, Figure 21 presents two cases where the

predicted crack pattern was different from the experimental observations. A typical unsuccessful failure mode is the "cross" tearing case, named after the shape of the torn part of the plate. All the models that failed to predict the correct crack pattern were using too high values of the threshold range. Low values of $D_{\min}$ and $D_{\max}$ result in large refined zones in the vicinity of the crack initiation, while high values of $D_{\min}$ and $D_{\max}$ limited the refinement zones immediately before crack formation and this may hamper the correct prediction of failure. Thus, Figure 20a indicates a good selection of threshold range parameters, which sufficiently refines the critical area just before crack initiation, while Figure 20b illustrates a combination which underestimates the area to be refined.

The adaptivity parameters able to reproduce the failure mode of the plates and the corresponding CPU cost are summarized in Table 6. The first columns in Table 6 show input parameters such as the base mesh size (L_{base}), the refinement level ($L^{s}_{\max}$) and the threshold range ($D_{\min}, D_{\max}$), while the last columns present data related to the CPU cost. The 6$^{\text{th}}$ column contains the number of elements used in the calculations, where the first number refers to the base mesh size and the second number gives the descendants generated in the refinement process. The CPU cost is proportional to both these numbers. The number of descendants influences the CPU cost from the moment that refinement starts until the end of the calculation. On the contrary, the number of base elements influences the CPU cost from the beginning of the calculation until the refinement starts. In an explicit FE simulation, the critical time step is conditioned by the smallest element in the model when the material properties are the same for all elements. Coarser base meshes imply larger time steps until adaptivity starts, resulting in lower CPU costs. The time step is the same for all the cases after activation of the refinement process.

Table 6 reveals that AMR reduced the CPU cost by 56 to 78 %. The set of values giving the best overall results is the one highlighted in bold in Table 6, corresponding to a base mesh

size of 6 mm and a reduction in CPU time of 68 %. This set of parameters predicts a crack growth similar to the uniformly refined (0.75mm) mesh model, as illustrated in Figure 22. Also the clamped assembly model using contact and AMR with the selected set of parameters successfully reproduces all the failure patterns observed in the experiments, either with partial tearing (P25) or with full tearing (P35), as shown in Figure 23. Thus, the use of AMR allows for an efficient and accurate model of the complete experimental assembly including the added complexity of the clamping system with contact and friction, something that would be unfeasible (or prohibitively CPU-expensive) with a uniformly refined mesh. The crack velocity in this simulation of test P35 was found to be 141.0 m/s (77 m/s), which was slightly larger than the experimental measurements in Section 3.2.

6. Concluding remarks

The dynamic response of blast-loaded steel plates has been studied both experimentally and numerically. Blast-like loadings were generated using a shock tube facility, where both massive and deformable steel plates were located at the tube end. The massive plate was used to obtain a rigid blind flange, while thin deformable plates (both with and without pre-formed holes) were used to introduce moving boundary conditions. Pressure measurements from the massive plate tests could then be used as a basis to investigate fluid-structure interaction (FSI) effects in the tests with deformable plates. Mid-point deflections during the deformable plate tests were measured using 3D-DIC, and these results were used to quantify the dynamic response of the thin steel plates during the shock tube tests. Special focus was placed on the influence of pre-formed holes on the dynamic response. Synchronization of 3D-DIC and pressure measurements enabled a thorough investigation of the experiments. The tests were performed at various blast intensities and covered a wide range of structural response from large inelastic deformations to complete tearing along the diagonals of the plates with holes.

FSI effects were investigated by comparing the loading on massive and flexible plates under similar blast-load conditions, and a trend of reduced reflected pressures was found when introducing pre-formed holes in the plates. The set of experimental data presented in this study therefore serves as a basis for evaluation of numerical methods to study the behaviour of flexible plates exposed to blast loading.

The capabilities of an uncoupled approach in predicting the experimental observations were evaluated using the FE code EUROPLEXUS (EPX). A purely Lagrangian method was used to investigate the influence of boundary conditions and mesh size on the dynamic response and failure of the plates, respectively. The loading measured during the massive plate tests was imposed as a uniformly distributed pressure on the exposed area of the deformable plates in the simulations. Thus, these simulations make the inherent assumption that the pressure is unaltered by the plate deformation and the pre-formed holes (if present). As expected, allowing for sliding at the supports resulted in larger mid-point deflections. This was most evident for the deformable plates without holes. Failure in the perforated plates was only predicted when using a mesh size similar to the plate thickness of 0.8 mm. However, such a uniformly refined mesh resulted in a significant increase of CPU cost. The capability of damage-based adaptive mesh refinement (AMR) in the plates was therefore investigated in an attempt to reduce the CPU cost. Mesh refinement was driven by the damage parameter D in the material model and occurred at user-defined levels of this parameter. It was found that the predicted failure patterns were highly dependent on the initial mesh size and damage threshold. By using an initial mesh size of 6 mm and three successive levels of refinement when $0.01 \leq D \leq 0.02$, the AMR model captured the same failure patterns as in the uniformly refined model with a 68 % reduction in CPU cost.

Even though the numerical results were encouraging, further investigations are needed to ensure an appropriate use of damage-based AMR in engineering applications. Moreover, a

tendency to overestimate the plate response for a given blast pressure when using uncoupled simulations was observed. This was most evident for the plates without holes and at increasing magnitudes of pressure. A plausible explanation for this observation is that the simulations assume a uniformly distributed pressure on the plate, neglecting FSI effects that reduce the reflected pressure acting on the plates. Numerical simulations of the perforated plates also show some overestimation of the response, but less than in the case of full plates, possibly due to the 16 % smaller active surface of the perforated plates. These observations are consistent with previous research which indicates that the accuracy of the uncoupled approach is dependent on the blast and structural properties. It is previously shown that the presence of FSI effects will reduce the transmitted impulse and the plate response. FSI effects are reported to be marginal at lower blast intensities, but may be considerable for high-intensity blast loading on lightweight structures. Thus, quantitatively more accurate results are expected using fully coupled simulations including the fluid and the resulting FSI effects. However, this is beyond the scope of this study and will therefore be investigated in further studies using the structure model calibrated in the present work.

Acknowledgement

This work has been carried out with financial support from the Structural Impact Laboratory (SIMLab), Centre for Research-based Innovation (CRI), at the Norwegian University of Science and Technology (NTNU), and at the Directorate for Space Security and Migration, Safety and Security of Buildings, at the Joint Research Centre (EC-JRC). The authors would like to express their gratitude to Mr. Trond Auestad and Mr. Tore Wisth from CRI-CASA for their contributions during the experimental work. Contributions from M.Sc. students Henrik Møgster Granum and Lars Marcus Løken are also greatly appreciated.

References

[1] X.-S. Kong, W.-G. Wu, J. Li, P. Chen, F. Liu. Experimental and numerical investigation on a multi-layer protective structure under the synergistic effect of blast and fragment loadings. International Journal of Impact Engineering 2014;65:146-162.

[2] G. S. Langdon, I. B. Rossiter, V. H. Balden, G. N. Nurick. Performance of mild steel perforated plates as blast wave mitigation technique: Experimental and numerical investigation. International Journal of Impact Engineering 2010; 37:1021-1036.

[3] G. S. Langdon, G. N. Nurick, N. J. du Plessis. The influence of separation distance on the performance of perforated plates as a blast wave shielding technique. Engineering Structures 2011;33:3537-3545.

[4] K. G. Rakvåg, N. J. Underwood, G. K. Schleyer, T. Børvik, O. S. Hopperstad. Transient pressure loading of clamped metallic plates with pre-formed holes. International Journal of Impact Engineering 2013;53:44-55.

[5] R. L. Veldman, J. Ari-Gur, C. Clum. Response of pre-pressurized reinforced plates under blast loading. International Journal of Impact Engineering 2008;35:240-250.

[6] K. P. Dharmasena, H. N. G. Wadley, K. Williams, Z. Xue, J. W. Hutchinson. Response of metallic pyramidal lattice core sandwich panels to high intensity impulsive loading in air. International Journal of Impact Engineering 2011;38:275-289.

[7] S. Chung Kim Yuen, G. N. Nurick, G. S. Langdon, Y. Iyer. Deformation of thin plates subjected to impulsive load: Part III – an update 25 years on. International Journal of Impact Engineering 2016. Article in Press. DOI:10.1016/j.ijimpeng.2016.06.010.

[8] K. Spranghers, I. Vasilakos, D. Lecompte, H. Sol, J. Vantomme, Numerical simulation and experimental validation of the dynamic response of aluminum plates under free air explosions, International Journal of Impact Engineering 2013;54:83-95.

[9] V. Aune, E. Fagerholt, K. O. Hauge, M. Langseth, T. Børvik. Experimental study on the response of thin aluminium and steel plates subjected to airblast loading. International Journal of Impact Engineering 2016;90:106-121.

[10] M. A. Louar, B. Belkassem, H. Ousji, K. Spranghers, D. Kakogiannis, L. Pyl and J. Vantomme. Explosive driven shock tube loading of aluminium plates: Experimental study. International Journal of Impact Engineering 2015;86:111-123.

[11] A. R. K. Chennamsetty, J. LeBlanc, S. Abotula, P. N. Parrikar and A. Shukla. Dynamic response of Hastelloy® X plates under oblique shocks: Experimental and numerical studies. International Journal of Impact Engineering 2015;85:97-109.

[12] V. Aune, E. Fagerholt, M. Langseth, T. Børvik. A shock tube facility to generate blast loading on structures. International Journal of Protective Structures 2016;7:340-366.

[13] US Army Corps of Engineers, Naval Facilities Engineering Command, Air Force Civil Engineer Support Agency. Structures to resist the effects of accidental explosions. UFC 3-340-02. Supersedes TM5-1300, dated November 1990. US Department of Defense, Washington, DC, December 2008.

[14] G. I. Taylor. The pressure and impulse of submarine explosion waves on plates. In: Batchelor, G. K. (Ed.), The Scientific Papers of Sir G. I. Taylor, Volume III: Aerodynamics and the Mechanics of Projectiles and Explosions. Cambridge University Press, pp. 287-303, 1963.

[15] N. Kambouchev, L. Noels, R. Radovitzky. Nonlinear compressibility effects in fluid-structure interaction and their implications on the air-blast loading of structures. Journal of Applied Physics 2006;100:063519.

[16] N. Kambouchev, L. Noels, R. Radovitzky. Fluid-structure interaction effects in the dynamic response of free-standing plates to uniform shock loading. Journal of Applied Mechanics 2007;74:1042-1045.

[17] A. Vaziri, J. W. Hutchinson. Metal sandwich plates subjected to intense air shocks. International Journal of Solids and Structures 2007;44:2021-2035.

[18] EUROPLEXUS user's manual, Joint Research Centre. http://europlexus.jrc.ec.europa.eu/public/manual_pdf/manual.pdf [accessed 19.03.2017].

[19] F. Casadei, P. Diez, F. Verdugo. An algorithm for mesh refinement and un-refinement in fast transient dynamics. International Journal of Computational Methods 2013; 10: 1-31.

[20] E. Fagerholt. Field measurements in mechanical testing using close-range photogrammetry and digital image analysis. PhD thesis. Norwegian University of Science and Technology, NTNU, Norway, 2012.

[21] Swedish Steel AB (SSAB), Docol DP/DL Cold reduced dual phase steels, SSAB Swedish Steel Ltd, http://www.ssab.com [cited 19.03.2017].

[22] J. K. Holmen, O. S. Hopperstad, T. Børvik, Low velocity impact on multi-layered dual-phase steel plates, International Journal of Impact Engineering 2015;78:161-177.

[23] G. Gruben, E. Fagerholt, O. S. Hopperstad, T. Børvik. Fracture characteristics of a cold-rolled dual-phase steel. European Journal of Mechanics A/Solids 2011;30:204-218.

[24] E. Fagerholt, T. Børvik, O. S. Hopperstad, Measuring discontinuous displacement fields in cracked specimens using Digital Image Correlation with mesh adaptation and crack-path optimization, Optics and Lasers in Engineering 2013;51:299-310.

[25] G. Gruben, M. Langseth, E. Fagerholt, O. S. Hopperstad. Low-velocity impact on high-strength steel sheets: An experimental and numerical study. International Journal of Impact Engineering 2016;88:153-171.

[26] K. V. Subramaniam, W. Nian, Y. Andreopoulos. Blast response simulation of an elastic structure: Evaluation of the fluid-structure interaction effect. International Journal of Impact Engineering 2009;36:965-974.

[27] V. Aune, G. Valsamos, F. Casadei, M. Larcher, M. Langseth, T. Børvik. Numerical study on the structural response of blast-loaded thin aluminium and steel plates. International Journal of Impact Engineering 2017;99:131-144.

[28] M. G. Cockcroft, D. J. Latham. Ductility and the workability of metals. Journal of the Institute of Metals 1968;96:33-39.

[29] S. Dey, T. Børvik, O. S. Hopperstad, M. Langseth. On the influence of fracture criterion in projectile impact of steel plates. Computational Materials Science 2006;38:176-191.

[30] T. Børvik, S. Dey, A. H. Claussen. Perforation resistance of five different high-strength plates subjected to small-arms projectiles. International Journal of Impact Engineering 2009;36:948-964.

[31] A. Kane, T. Børvik, A. Benallal, O. S. Hopperstad. Failure criteria with unilateral conditions for simulation of plate perforation. European Journal of Mechanics – A/Solids 2011;30:468-476.

[32] J. K. Holmen, J. Johnsen, O. S. Hopperstad, T. Børvik. Influence of fragmentation on the capacity of aluminium alloy plates subjected to ballistic impact. European Journal of Mechanics A/Solids 2016;55:221-233.

[33] G. S. Langdon, W. C. Lee, L. A. Louca. The influence of material type on the response of plates to air-blast loading. International Journal of Impact Engineering 2015;78:150-160.

[34] Livermore Software Technology Corporation (LSTC), http://www.lstc.com [accessed 19.03.2017].

[35] Cast3m software: http://www-cast3m.cea.fr/ [accessed 19.03.2017].

[36] ParaView software: http://www.paraview.org/ [accessed 19.03.2017].

[37] European Committee for Standardization (CEN). NS-EN 1090-2:2008+A1:2011, Execution of steel structures and aluminium structures - Part 2: Technical requirements for steel structures; 2008.

[38] C. Ruggieri, T. L. Panontin, R. H. Dodds Jr. Numerical modelling of ductile crack growth in 3-D using computational cell elements. International Journal of Fracture 1996;82:67-95.

[39] T. Belytschko, M.O. Neal. Contact-impact by the pinball algorithm with penalty and Lagrangian methods. International Journal for Numerical Methods in Engineering 1991;31:547-572.

[40] T. Belytschko, I.S. Yeh. The splitting pinball method for contact-impact problems. Computer methods in Applied Mechanics and Engineering 1993;105:375-393.

[41] J. M. Biggs. Introduction to structural dynamics. New York, McGraw-Hill, 1964.

[42] W. E. Baker, P. A. Cox, P. S. Westine, J. J. Kulesz, R. A. Strehlow. Explosion hazards and evaluation. Elsevier, Amsterdam, 1983.

[43] T. Krauthammer. Modern protective structures. CRC Press, Taylor & Frances Group, 2001.

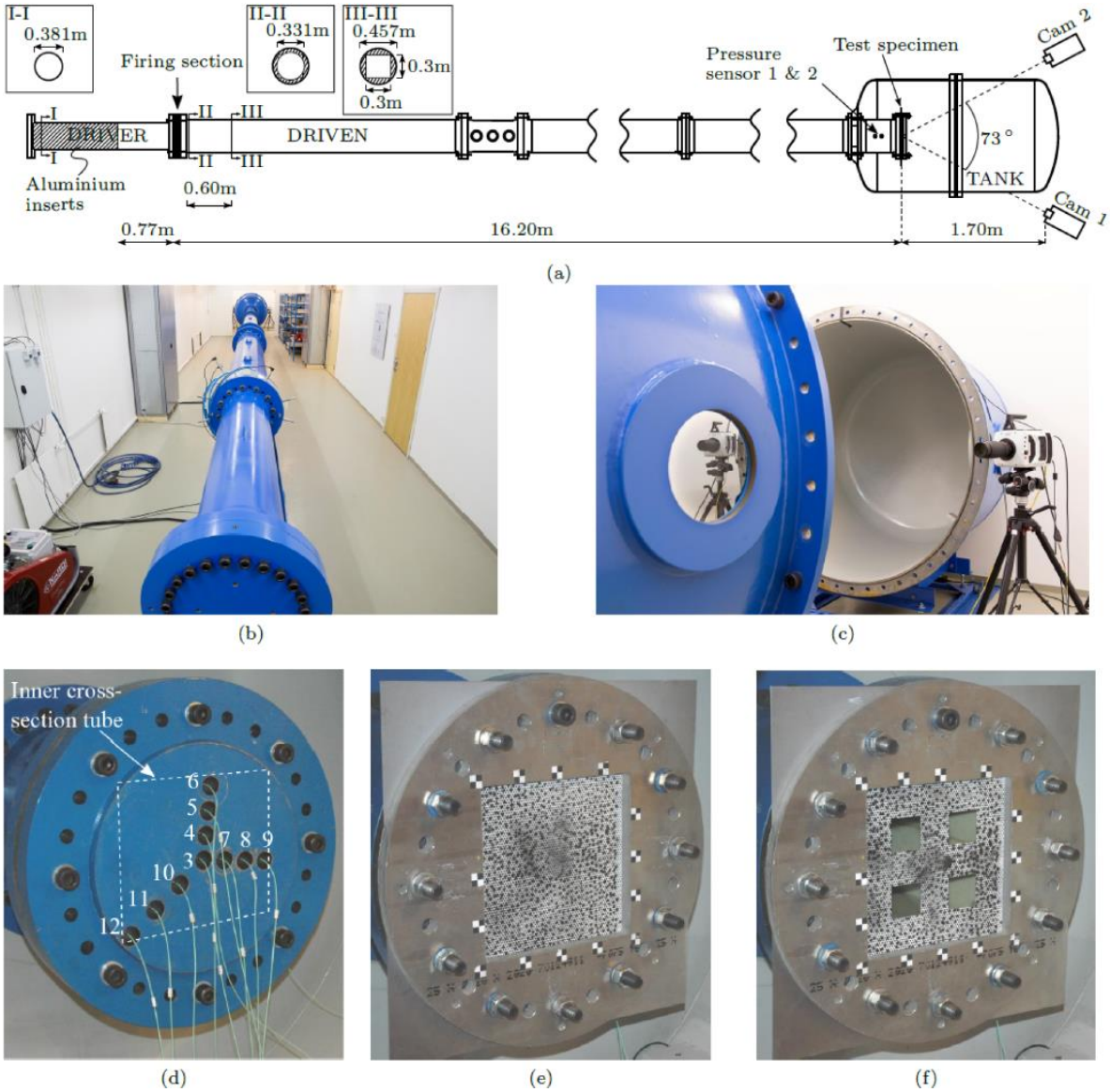

Figure 1. Experimental setup of the SIMLab Shock Tube Facility (SSTF): (a) Sketch of experimental setup (seen from above), (b) the shock tube (seen from the driver), (c) high-speed cameras next to the tank, (d) massive steel plate, (e) picture of clamping and DIC speckle pattern for the flexible steel plate and (f) clamping of plate with pre-formed holes. Both the massive steel plate in (d) and the flexible steel plates in (e) and (f) are seen from the cameras.

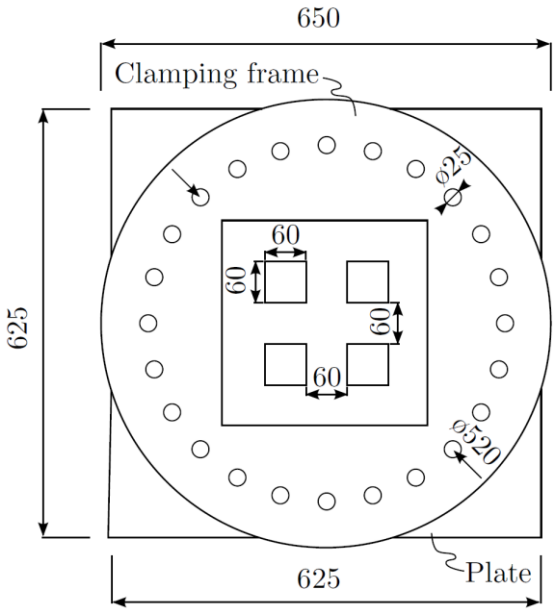

Figure 2. Geometry of the clamping assembly and position of the pre-formed holes. All measures in mm.

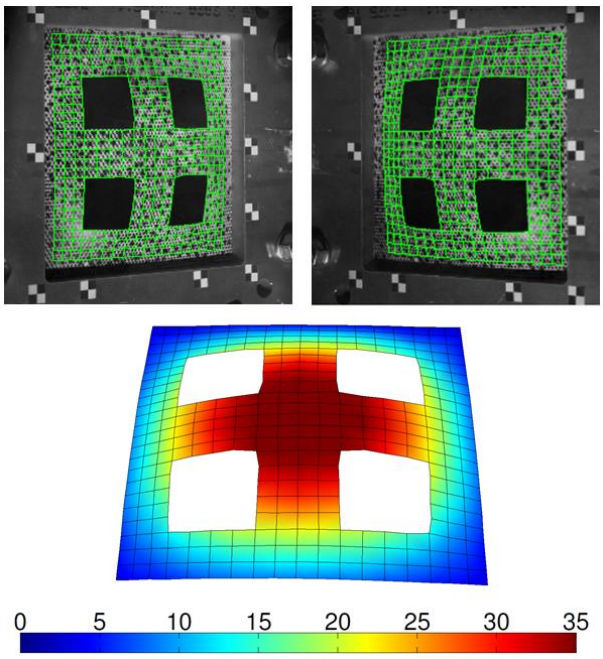

Figure 3. Results from 3D-DIC in test P25-02. The resulting DIC mesh is plotted on top of the recorded images from camera 1 (top left) and camera 2 (top right), while the corresponding 3D model from DIC is presented in the lower image. The colour scaling on the 3D-model indicates out-of-plane displacements (in mm).

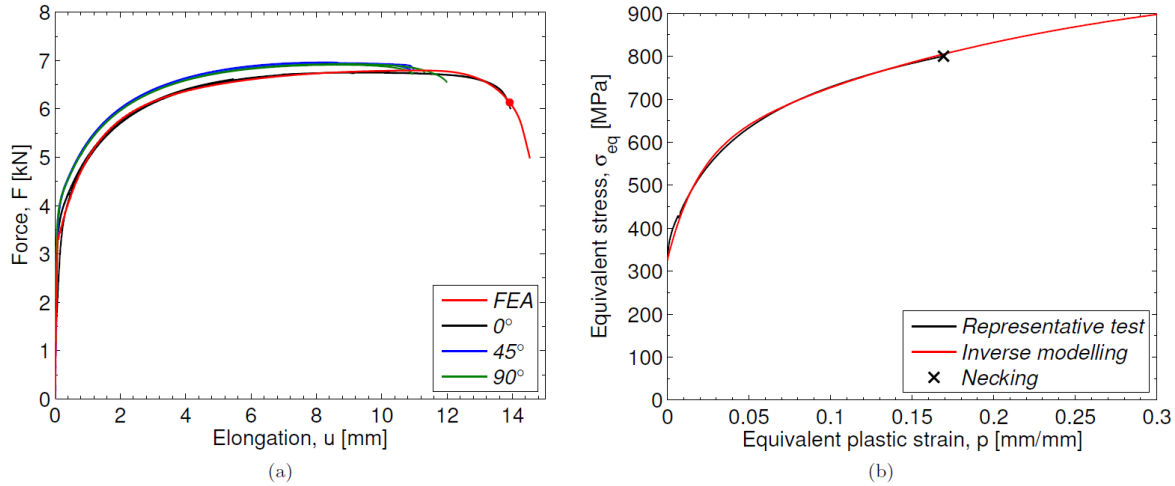

Figure 4. (a) Force-elongation curves from uniaxial tensile tests along three different loading directions. The corresponding finite element solution from EPX with the material data from Table 3 and Table 4 are included for comparison. The red dot illustrates the point of failure in the calculation of W_c. (b) Equivalent stress-plastic strain curves until necking for the representative test in the rolling direction, and the extended Voce hardening rule based on the material parameters from the inverse modelling in Table 3.

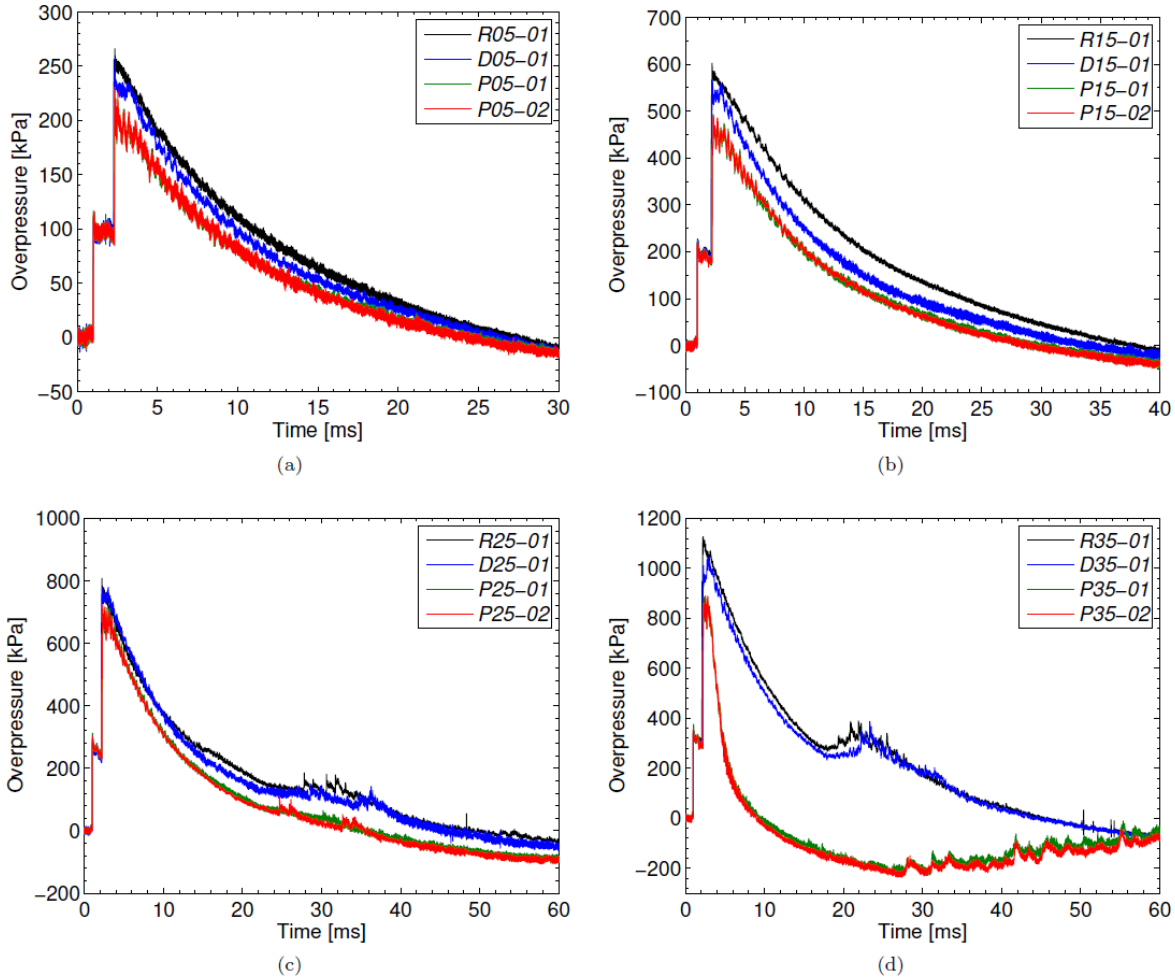

Figure 5. Comparison of pressure histories at Sensor 2 for massive and deformable plates exposed to similar blast intensities.

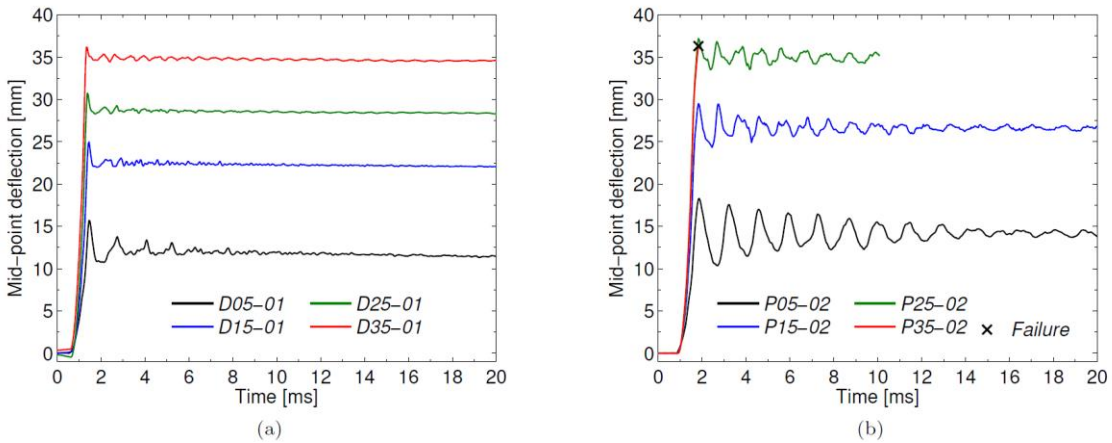

Figure 6. Mid-point deflection based on the 3D-DIC measurements: (a) Plates without holes and (b) plates with pre-formed holes. All curves are corrected for the rigid body movement of the shock tube. Also note that the curves are shifted in time to match the time of impact. The black marker illustrates the point of complete failure in P35-02.

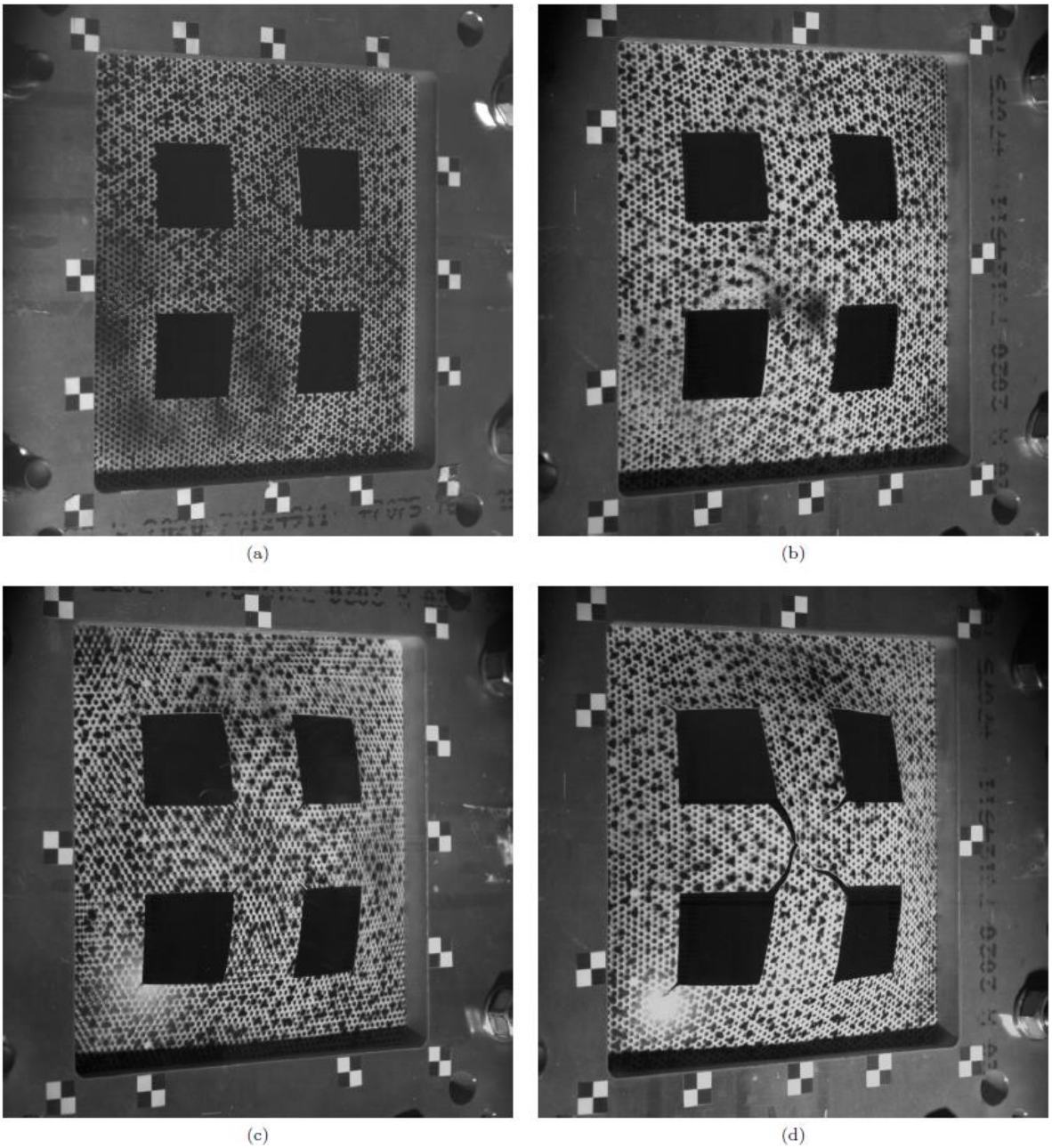

Figure 7. High-speed images at maximum mid-point deflection for representative plates with pre-formed holes: (a) P05-02, (b) P15-02, (c) P25-02 and (d) P35-02.

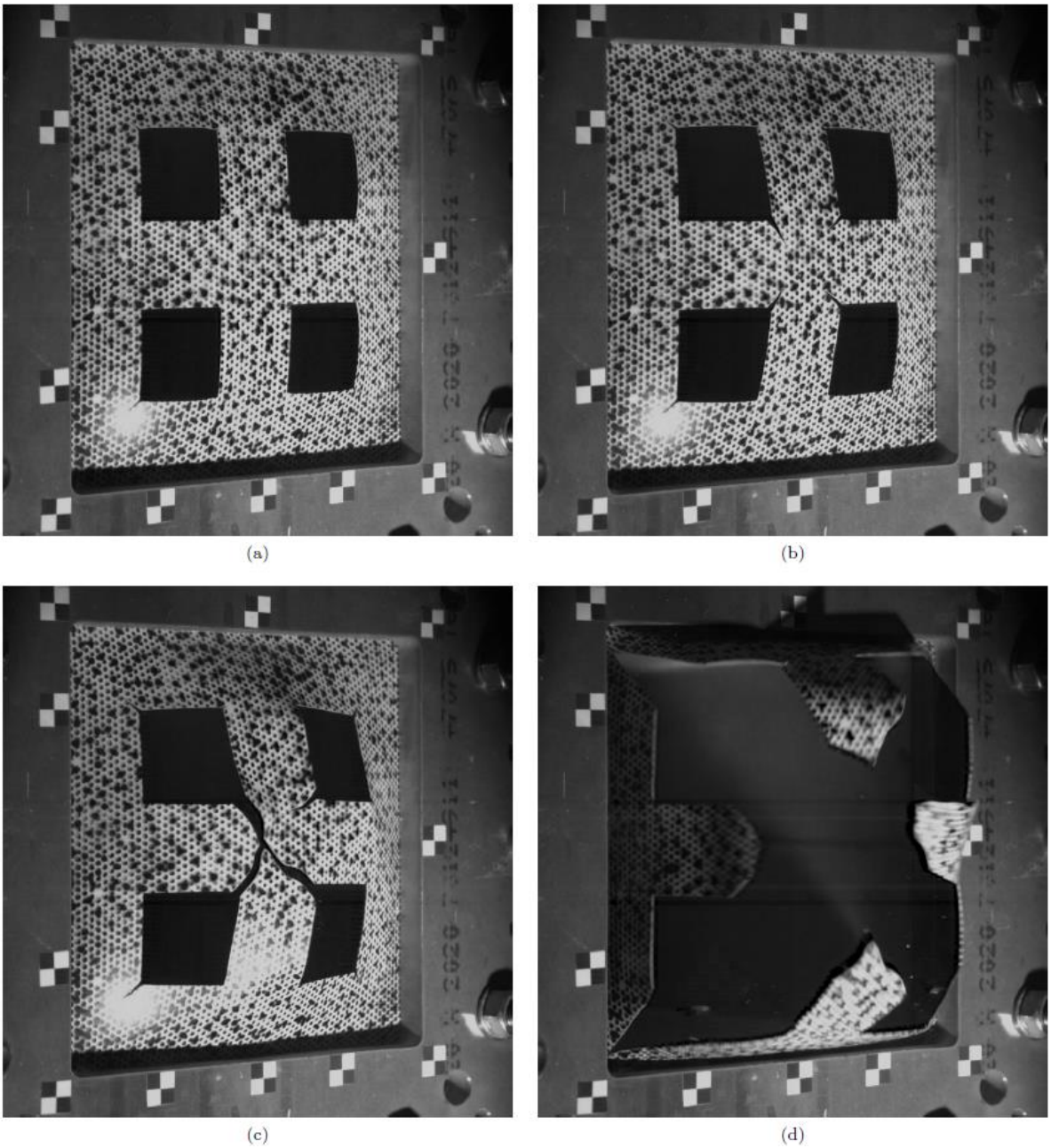

Figure 8. High-speed images of the failure process in test P35-02: (a) Failure first initiates along the diagonal in the outer corners of the holes (t = 1.13 ms), (b) before it propagates towards the centre (t = 1.42 ms). (c) The cracks eventually meet in the centre (t = 1.75 ms), and (d) propagate towards the outer corners of the plate resulting in complete tearing (t = 2.63 ms). Note that the respective times correspond to the shifted time in Figure 7b.

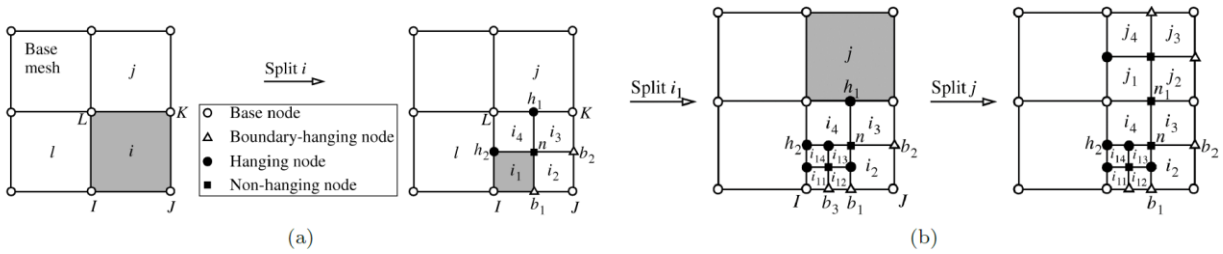

Figure 9. Illustration of the adaptive mesh refinement: (a) Splitting of a quadrilateral and (b) further splitting.

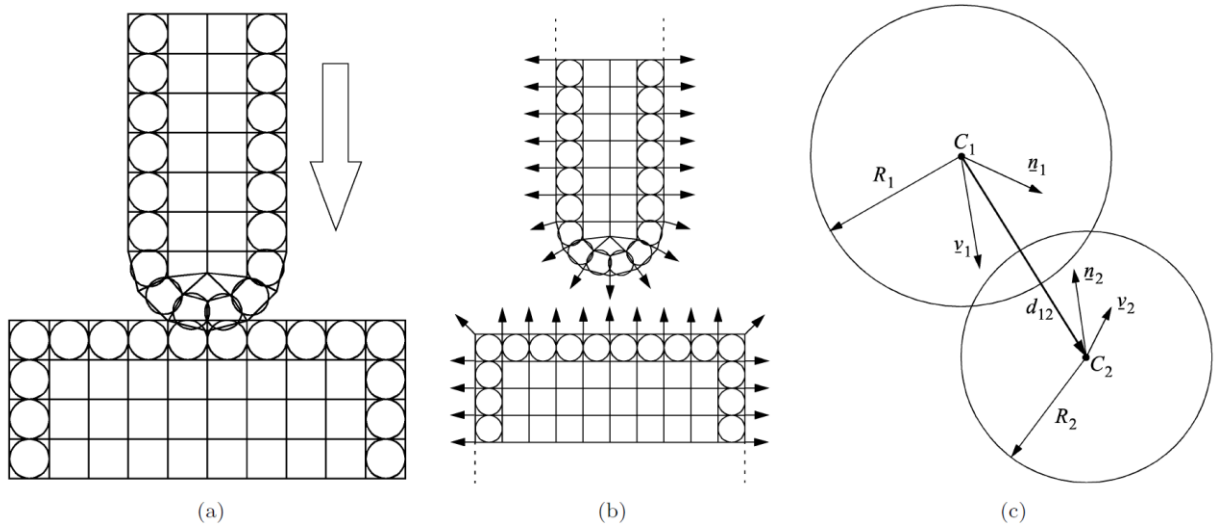

Figure 10. The basic pinball method illustrated in 2D for impact and penetration between quadrilateral continuum elements: (a) the pinball concept, (b) assembled surface normal and (c) interpenetrating pinballs.

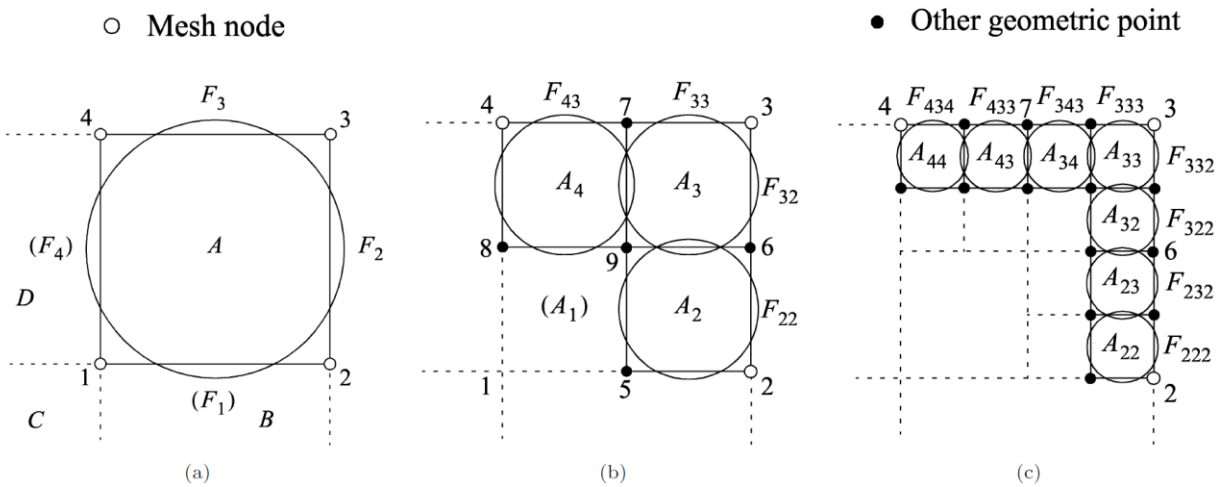

Figure 11. The hierarchic pinball method illustrated in 2D for quadrilateral continuum elements: (a) Level 0, (b) Level 1 and (c) Level 2.

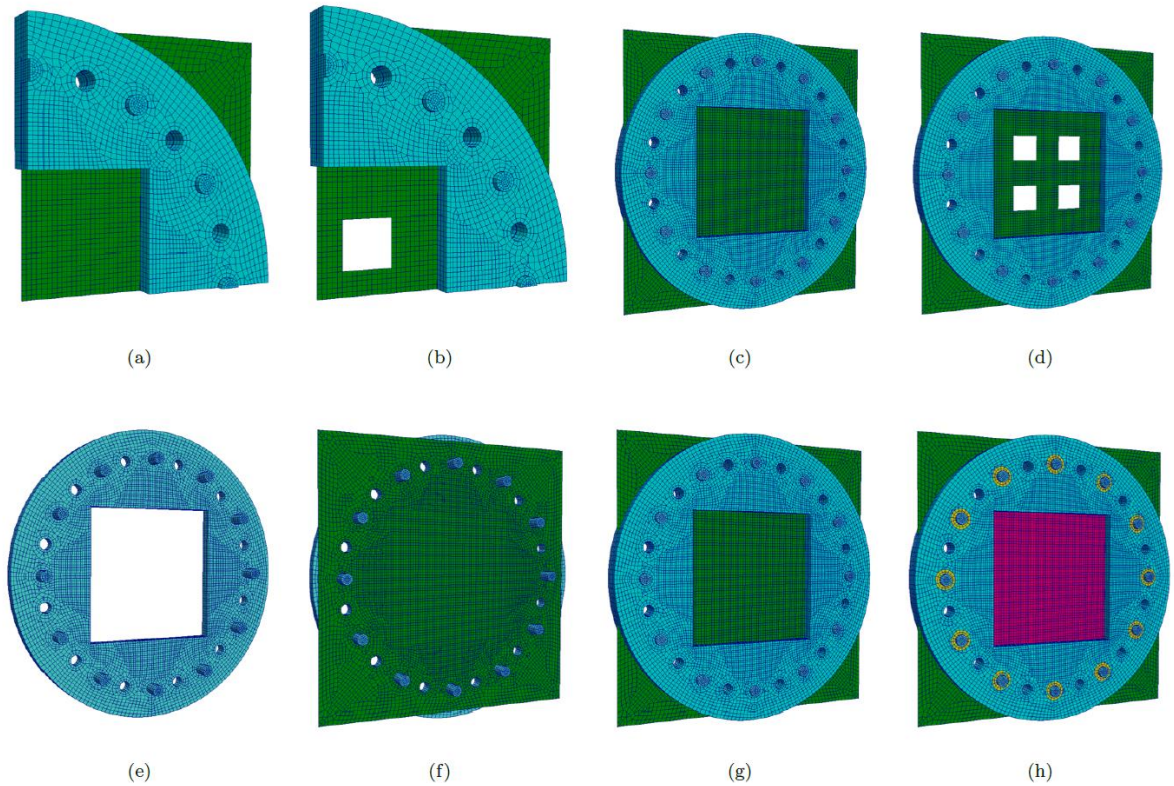

Figure 12. Numerical model showing the quarter model for (a) full and (b) perforated plate. The complete assembly is also shown after using mirror graphical functions in (c) full and (d) perforated plate, (e) steel mounting frame and the bolts as one component (in cyan), (f) full plate specimen is added (in green), (g) clamping frame is added (in cyan), (h) complete assembly for full plate specimen with the contact area between the bolt heads and the clamping frame shown in yellow and the exposed plate area in magenta.

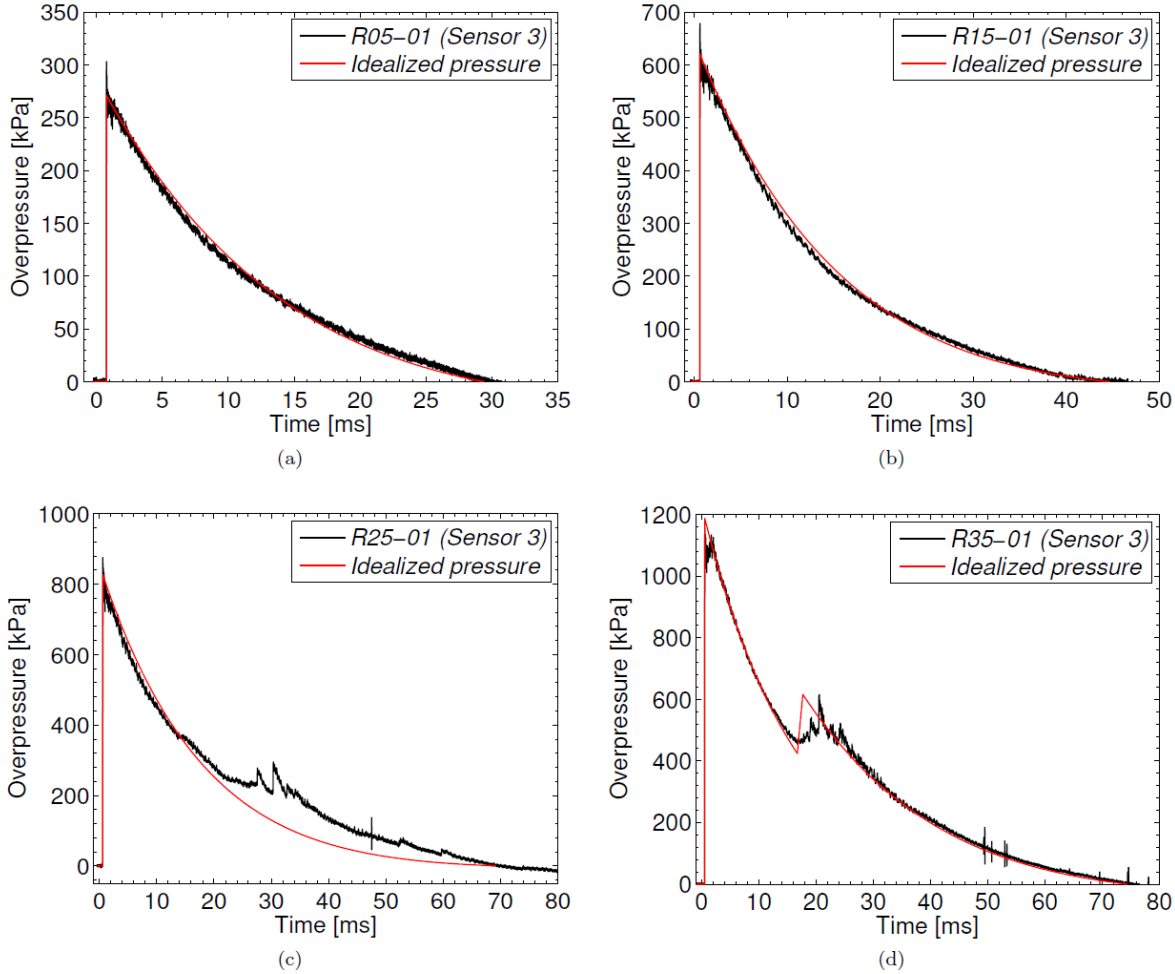

Figure 13. Pressure histories form the massive-plate tests: (a) R05, (b) R15, (c) R25 and (d) R35. The idealized curves were used in the simulations and found using curve-fitting to the experimental data at Sensor 3.

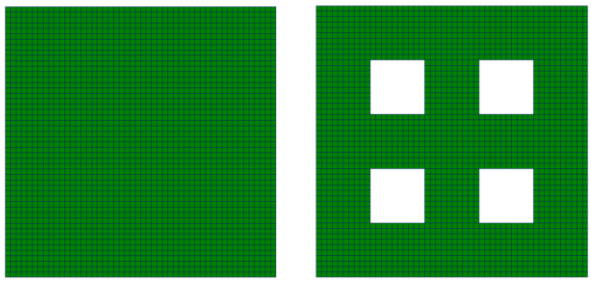

Figure 14. Simplified model using only the exposed area of the plate for (a) the full and (b) the perforated plate. The plates are fully restrained against translation and rotation along its perimeter.

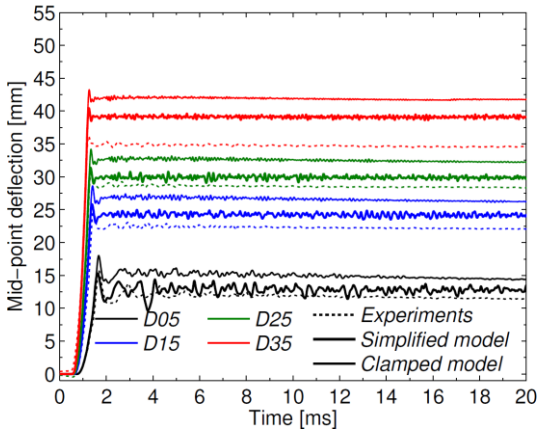

Figure 15. Mid-point deflection histories for the full-plate tests using a coarse mesh (6 mm). Comparison between experimental (dashed curves) and numerical results (thick solid curves for simplified model and thin solid curves for clamped assembly model) for tests D05, D15, D25 and D35.

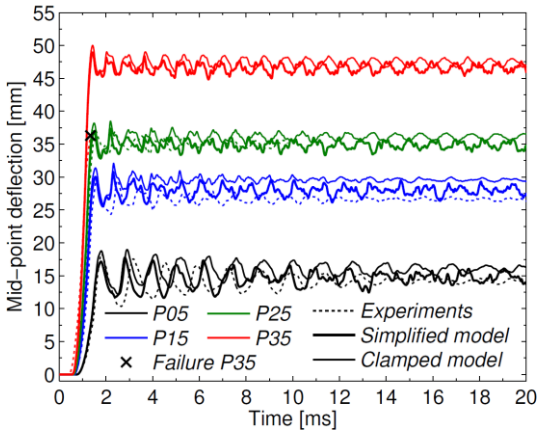

Figure 16. Mid-point deflection histories for the perforated plate tests using a coarse mesh (6 mm). Comparison between experimental (dashed curves) and numerical results (thick solid curves for simplified model and thin solid curves for clamped assembly model) for tests P05, P15, P25 and P35.

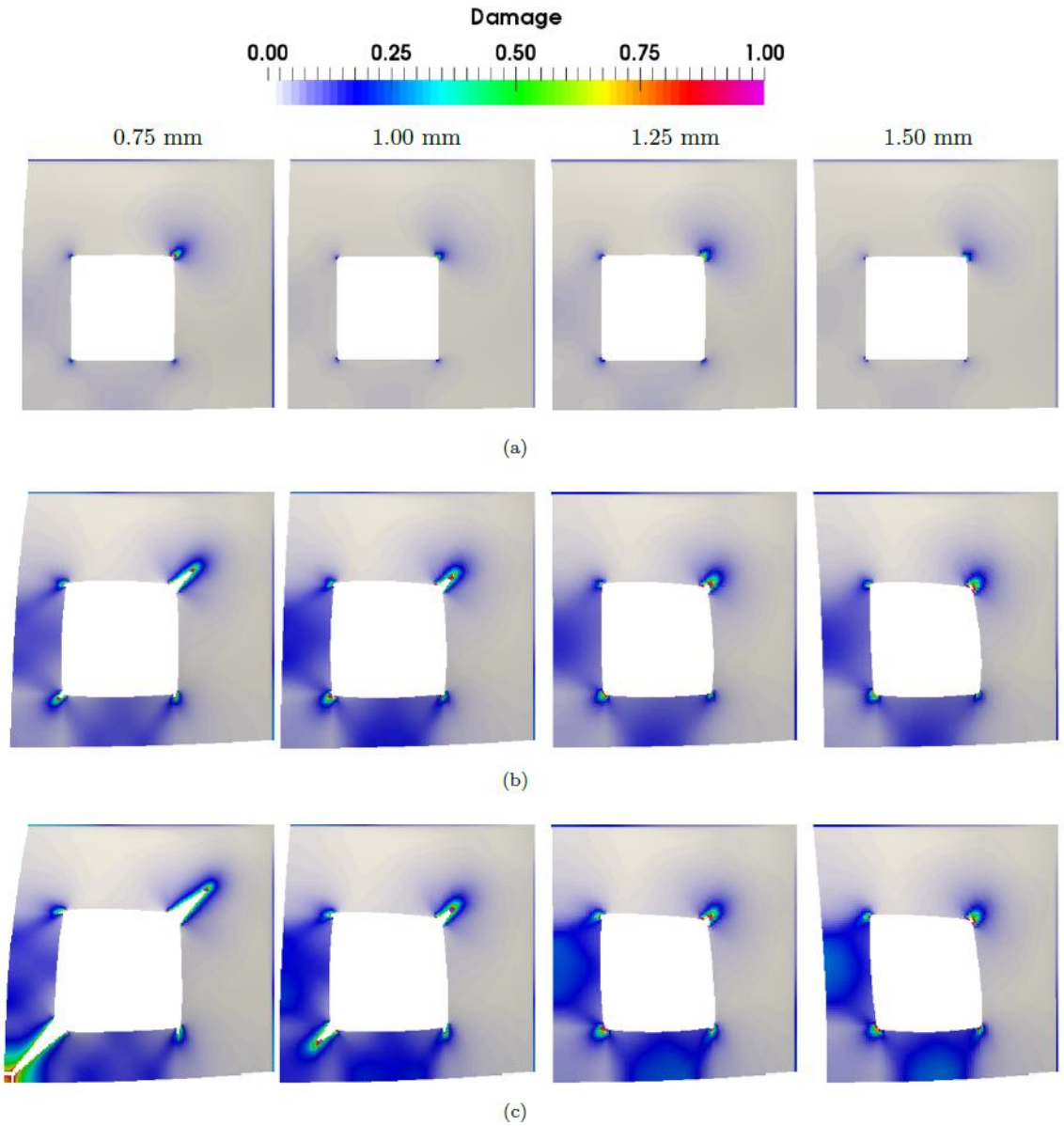

Figure 17. Comparison of damage evolution in test P35 for several mesh sizes (uniformly refined model): (a) Crack initiation at $t = 0.9$ ms, (b) crack growth at $t = 1.2$ ms and (c) $t = 1.4$ ms. Fringe colours represents the damage parameter in Eq. (5).

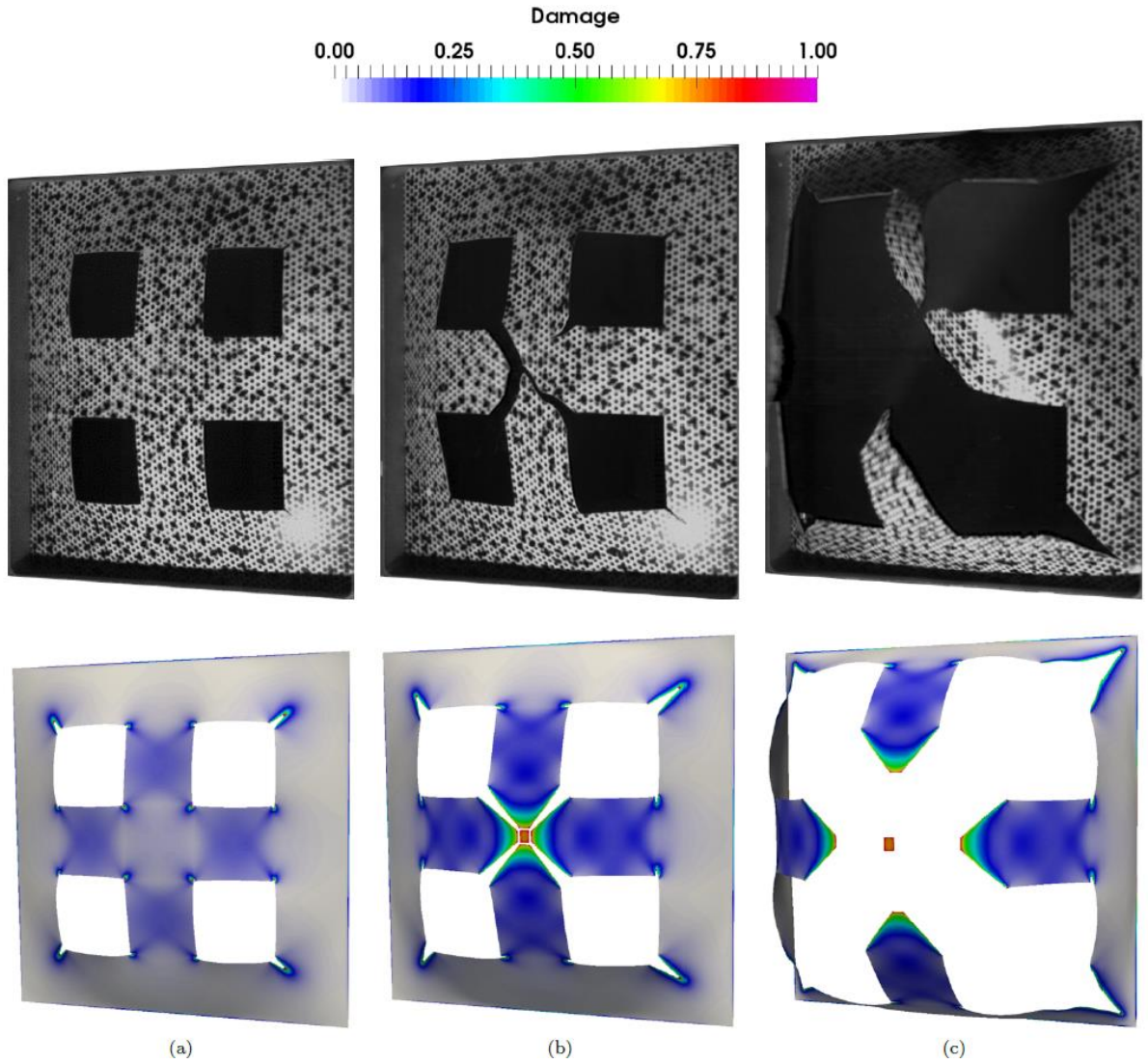

Figure 18. Comparison between the experimental observations (top row) and the damage evolution in the numerical model with uniform 0.75 mm mesh (bottom row) for test P35: (a) $t = 1.18$ ms, (b) $t = 1.52$ ms and (c) $t = 2.18$ ms. Fringe colours represents the damage parameter in Eq. (5).

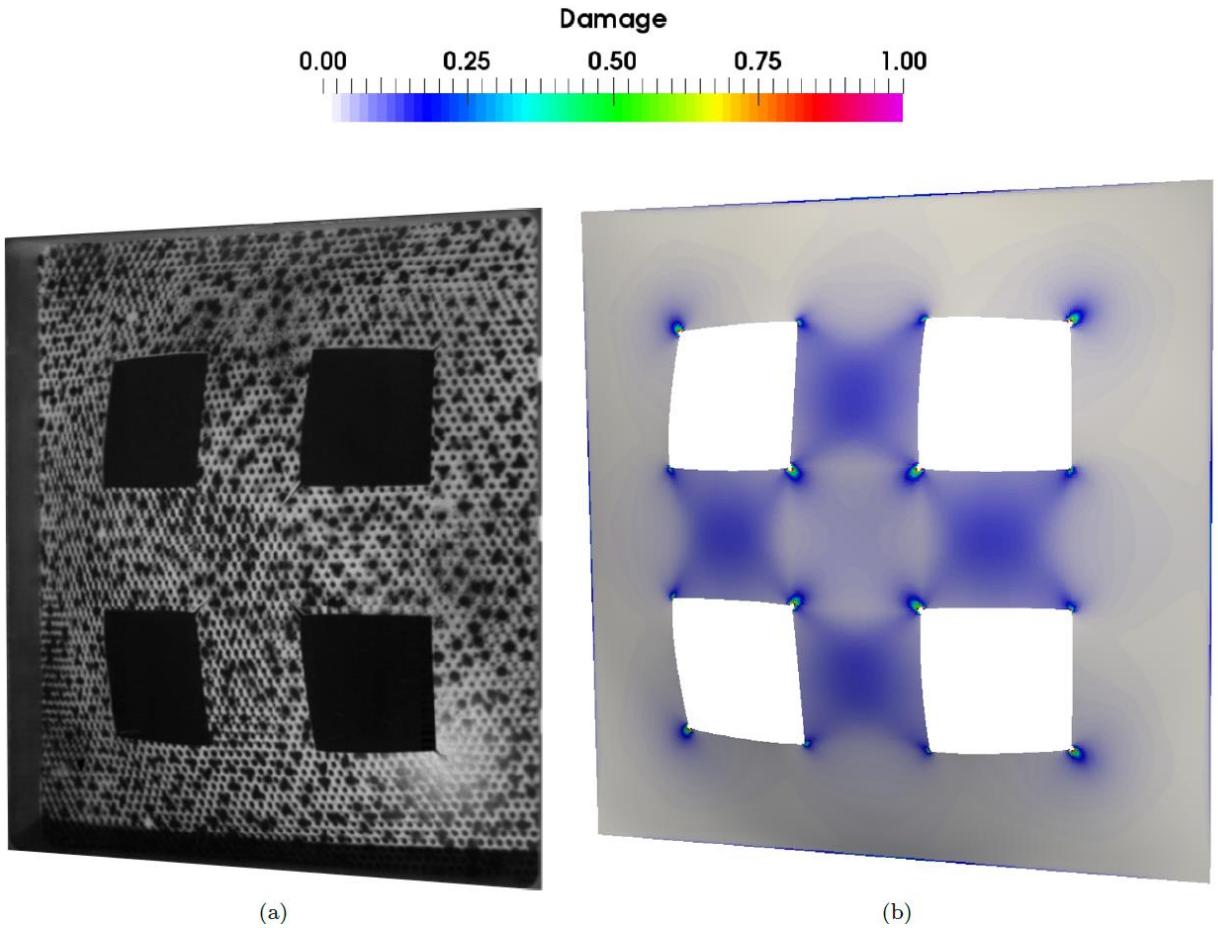

Figure 19. Comparison between (a) experimental observation and (b) damage evolution in the numerical model with 0.75 mm uniform mesh for the permanent configuration in test P25. Fringe colours represents the damage parameter in Eq. (5).

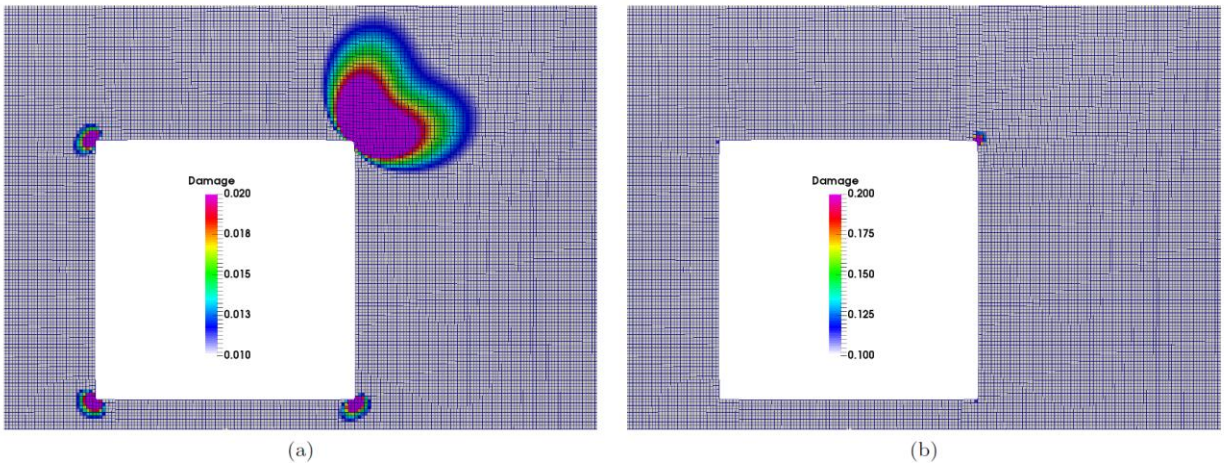

Figure 20. Damage contour maps for test P35 on the uniformly refined (0.75 mm) simplified model. The contour maps are obtained with two different scales at the same time instant just before crack initiation: (a) $0.01 < D < 0.02$ and (b) $0.10 < D < 0.20$. Only the mesh in the vicinity of the upper right hole of the plate is visualized. Fringe colours represents the damage parameter in Eq. (5).

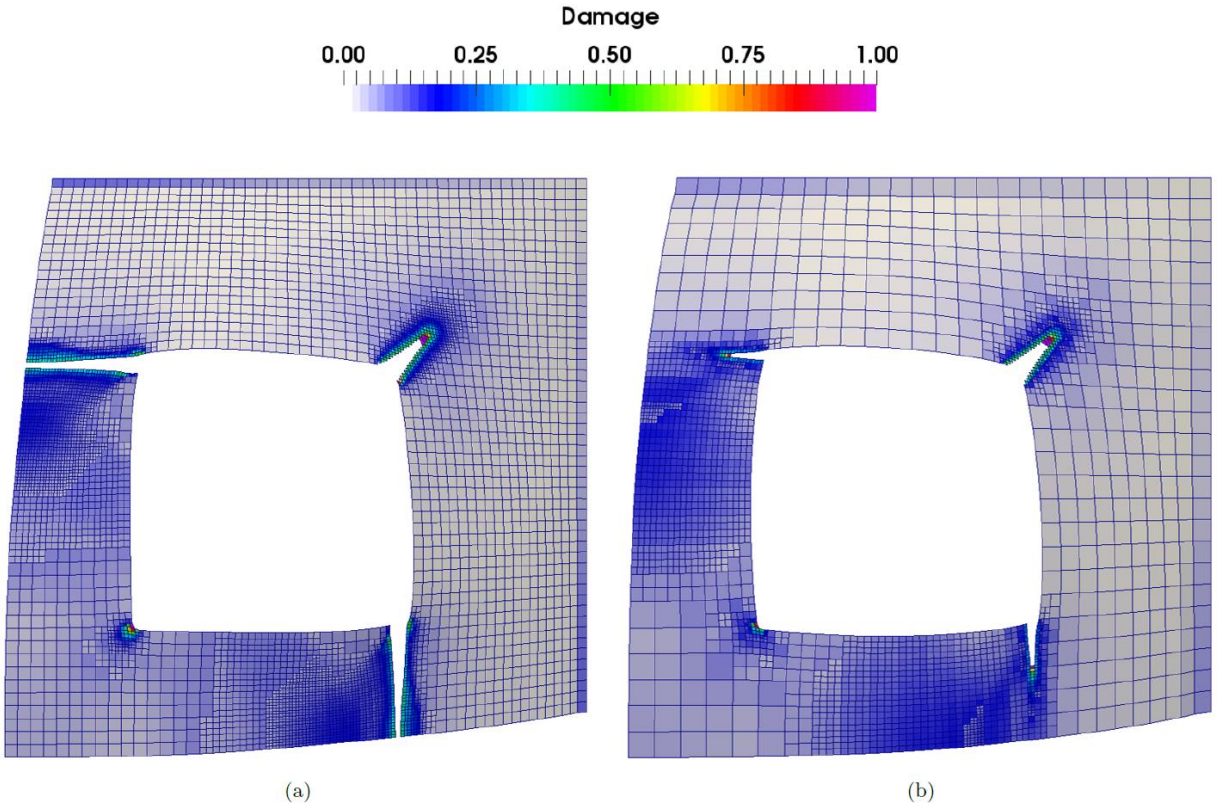

Figure 21. Two cases in which the AMR for the simplified model do not predict the correct failure pattern for test P35: (a) “Cross” tearing case and (b) non-tearing case. Fringe colours represents the damage parameter in Eq. (5).

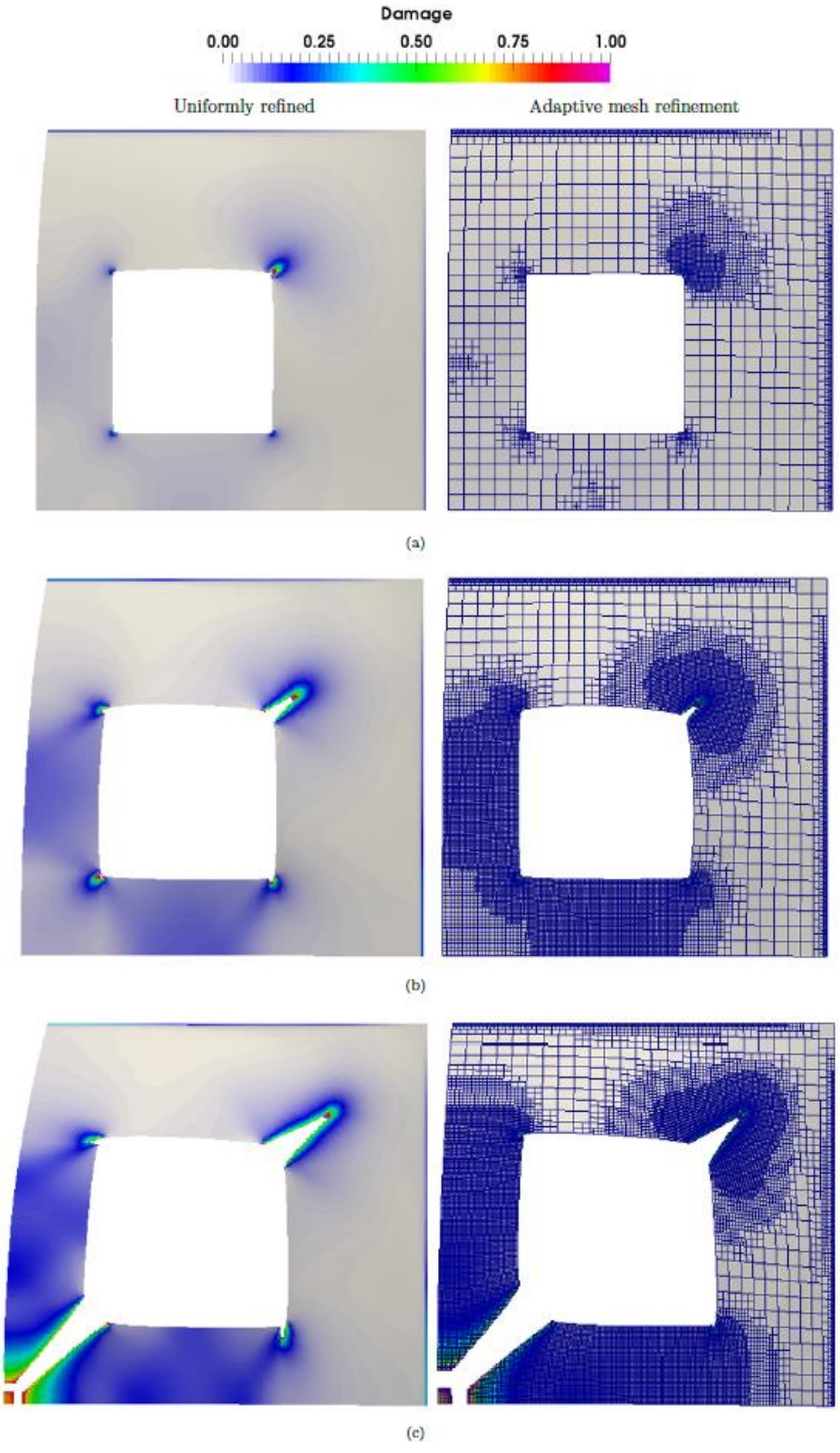

Figure 22. Crack growth in test P35 for the simplified model with 0.75 mm uniformly refined mesh (left) and the chosen adaptive model (right): (a) Crack initiation at $t = 0.9$ ms, (b) crack growth at $t = 1.1$ ms and (c) complete tearing at $t = 1.5$ ms. Only one quarter of the plate is presented in this figure. Fringe colours represents the damage parameter in Eq. (5).

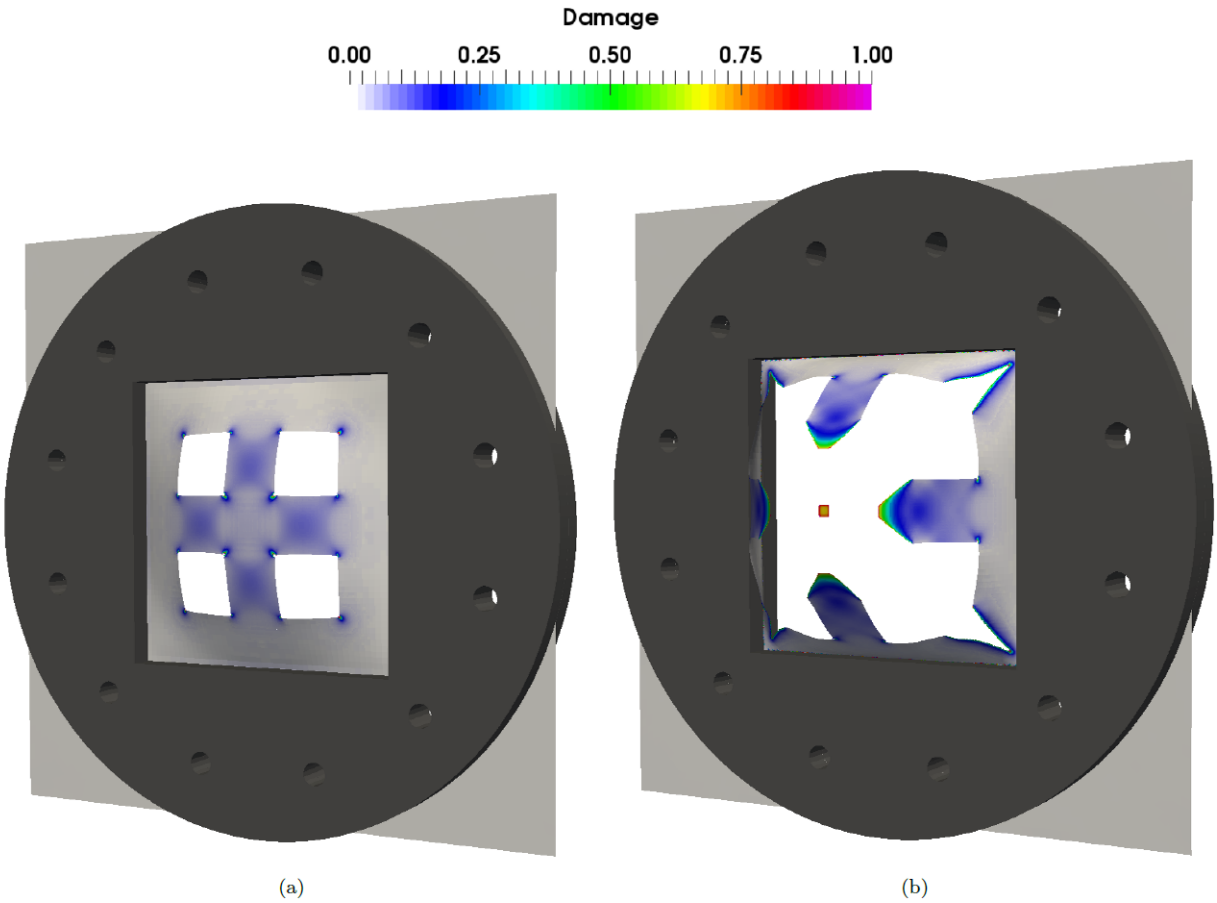

Figure 23. Failure patterns obtained with the AMR model of the clamped assembly with contact and friction: (a) test P25 with crack initiation near the hole extremities and (b) test P35 with complete tearing along the diagonals.

Post-print version of the paper by Aune et al. in Int J Impact Eng, 108 (2017) 27-46
http://dx.doi.org/10.1016/j.ijimpeng.2017.04.001

Table 1. Experimental programme.

Test	Initial conditions		
	Pressure driver [kPa]	Pressure driven [kPa]	Ambient temperature [ºC]
R05-01	618.5	99.7	22.0
R15-01	1594.0	99.8	24.0
R25-01	2821.6	99.7	23.9
R35-01	3811.8	99.8	23.6
D05-01	616.9	100.5	21.9
D15-01	1683.8	100.8	22.4
D25-01	2715.9	100.8	22.5
D35-01	3793.1	100.7	24.2
P05-01	622.7	100.5	22.1
P05-02	618.4	100.5	22.4
P15-01	1638.8	100.4	21.4
P15-02	1660.0	100.8	21.9
P25-01	2738.1	100.7	22.0
P25-02	2697.5	100.7	23.1
P35-01	3801.0	100.3	22.0
P35-02	3778.8	100.7	23.5

Table 2. Comparison of experimental and numerical results in terms of mid-point deflections and velocities ($\Delta d_{z,exp} = (d_{z,max} - d_{z,p}) / d_{z,max} \times 100\%$ and $\Delta d_z = (d_{z,max,exp} - d_{z,max,num}) / d_{z,max,exp} \times 100\%$).

Test	Experimental results				Numerical results							
					Clamped assembly				Simplified model			
	$d_{z,max}$ [mm]	$d_{z,p}$ [mm]	$\Delta d_{z,exp}$ [%]	$v_{z,max}$ [m/s]	$d_{z,max}$ [mm]	$d_{z,p}$ [mm]	Δd_z [%]	$v_{z,max}$ [m/s]	$d_{z,max}$ [mm]	$d_{z,p}$ [mm]	Δd_z [%]	$v_{z,max}$ [m/s]
D05-01	15.7	11.4	27.4	43.7	18.0	14.1	-14.6	51.2	15.3	12.5	1.5	39.9
D15-01	25.0	22.1	11.6	71.3	28.6	26.1	-12.4	83.9	25.8	24.3	-3.2	72.0
D25-01	30.8	28.4	7.8	91.6	34.1	32.1	-10.7	101.6	31.4	29.7	-1.9	89.4
D35-01	36.2	34.6	4.4	103.4	43.2	41.6	-19.3	131.8	40.4	39.2	-11.6	117.7
P05-01	18.3	14.4	21.3	41.6	18.7	16.1	-2.1	44.8	17.7	14.6	3.3	39.2
P05-02	18.3	14.2	22.4	41.6	18.7	16.1	-2.1	44.8	17.7	14.6	3.3	39.2
P15-01	29.2	26.2	10.3	71.6	31.3	29.6	-7.1	77.7	30.0	28.6	-2.7	71.9
P15-02	29.5	26.6	9.8	71.6	31.3	29.6	-6.1	77.7	30.0	28.6	-1.7	71.9
P25-01	36.2	33.8	6.6	86.4	38.2	36.0	-5.5	97.6	37.0	34.3	-2.2	89.6
P25-02	37.2	34.9	6.2	89.2	38.2	36.0	-2.6	97.6	37.0	34.3	0.5	89.6
P35-01	N/A*	N/A*	N/A*	100.5	N/A*	N/A*	N/A*	130.2	N/A*	N/A*	N/A*	122.7
P35-02	N/A*	N/A*	N/A*	87.5	N/A*	N/A*	N/A*	130.2	N/A*	N/A*	N/A*	122.7

*Experiment resulted in complete failure along the diagonal

Table 3. Calibrated material parameters for the extended Voce hardening rule and the CL failure criterion.

σ_0 [MPa]	Q_1 [MPa]	C_1 [-]	Q_2 [MPa]	C_2 [-]	W_c [MPa]
325.7	234.8	56.2	445.7	4.7	555.0

Table 4. Physical constants and material parameters taken from the literature [25][22][27].

E [GPa]	ν [-]	ρ [kg/m^3]	C_p [J/kg K]	$\dot{p}_0$ [s^{-1}]	c [-]	χ [-]	T_r [K]	T_m [K]	m [-]
210.0	0.33	7850	452	5×10^{-4}	0.01	0.9	293	1800	1.0

Table 5. Idealized pressure histories in terms of Friedlander parameters curve-fitted to the pressure measurements in the massive-plate tests in Figure 13 [12].

Test	$p_{r,max}$ [kPa]	t_{d+} [ms]	i_{r+} [kPa ms]	b [-]
R05	267.5	28.7	2557.9	1.306
R15	606.6	44.1	7510.0	2.025
R25	795.2	68.7	12,383.3	2.044
R35*	1105.2	73.9	16,613.4	1.904

*Only valid until secondary reflection at 17.20 ms. Use $p_{r,max} = 616$ kPa, $t_{d+} = 56.7$ ms and $b = 1.600$ after this point in time.

Table 6. Adaptivity parameters and corresponding CPU cost for the simulations predicting the failure mode for the P35 test. The case selected in this study is given in bold.

Initial mesh L_{base} [mm]	Refinement Level L^s_{max}	D_{min}	D_{max}	Refined mesh L_{UR} [mm]	Number of Elements	CPU time [s]	CPU reduction [%]
0.75	-	-	-	0.75	33,600	21,049	-
3	3	0.005	0.02	0.75	2,100+28,696	10,476	50
3	3	0.005	0.05	0.75	2,100+19,587	6,707	68
3	3	0.01	0.02	0.75	2,100+26,664	9,295	56
3	3	0.01	0.05	0.75	2,100+19,076	6,456	69
3	3	0.02	0.05	0.75	2,100+18,516	6,287	70
6	4	0.005	0.01	0.75	525+29,148	9,116	57
6	4	0.005	0.02	0.75	525+24,228	7,232	66
6	4	0.005	0.05	0.75	525+17,112	4,797	77
6	**4**	**0.01**	**0.02**	**0.75**	**525+22,756**	**6,655**	**68**
6	4	0.01	0.05	0.75	525+16,940	4,684	78